AN ABSTRACT OF THE THESIS OF

Anson M. Antriasian for the degree of Master of Science in Ocean, Earth, and Atmospheric Sciences presented on November 22, 2016.

Title: Crustal Heat flow and Thermal Modeling of the Hikurangi Trough, New Zealand

Abstract approved:

_____

Robert N. Harris

Measuring surface heat flow at the Hikurangi Trough is key toward characterizing the local thermal regime and the influence of thermally sensitive processes such as fluid flow and slow slip. Marine heat flow data were collected during May–June 2015 in the northern Hikurangi Trough at sites seaward and landward of the deformation front, giving mean and one standard deviation values of 58 ± 16 and 46 ± 15 mW m^{-2} respectively. A 3.5 m violin-bow style probe was used to measure thermal conductivity and temperature gradient of the seafloor, and heat flow is calculated using Fourier's law. Two-dimensional steady-state, finite element modeling was undertaken to analyze the influence of subduction parameters on surface heat flow and temperature along the subduction thrust. Heat flow values seaward of the deformation front have been found to be sensitive to the structure of buried and outcropping extrusive crust, but the mean heat flow is within the range of expected values for lithosphere this age (120 Myr) according to the GDH1 cooling model. Landward of the deformation front, measured heat

flow is in excess of preferred modeled values. I interpret these observations as evidence for fluid flow within a crustal aquifer system and through splay faults within the forearc. A heat flow discontinuity of 40 mW m^{-2} landward of the deformation front supports the presence of compaction sourced fluid along the subduction thrust, which is consistent with previous evidence for excess pore pressure and the occurrence of shallow slow slip.

Crustal Heat Flow and Thermal Modeling of the Hikurangi Trough, New Zealand

by

Anson M. Antriasian

A THESIS

submitted to

Oregon State University

in partial fulfillment of
the requirements for the
degree of

Master of Science

Presented November 22, 2016
Commencement June 2017

Master of Science thesis of Anson M. Antriasian presented on November 22, 2016

APPROVED:

Major Professor, representing Ocean, Earth, and Atmospheric Sciences

---

Dean of the College of Earth, Ocean, and Atmospheric Sciences

---

Dean of the Graduate School

I understand that my thesis will become part of the permanent collection of Oregon State University libraries. My signature below authorizes release of my thesis to any reader upon request.

Anson M. Antriasian, Author

ACKNOWLEDGEMENTS

The author is grateful for the contribution that his advisors Robert Harris and Anne Trehu have had towards the organization of the research cruise RR 1508 in the Hikurangi Trough and for their work in guiding his scientific thinking and writing. The author is also grateful to Stuart Henrys for his assistance with the seismic data used in this study.

TABLE OF CONTENTS

LIST OF FIGURES

LIST OF TABLES

Table Page

1. Introduction

The thermal regime of subduction zones has a strong influence on subduction processes. At temperature greater than about 300°C, the thermal regime influences rheology and crustal dehydration of the subducting slab. At cooler temperatures (< 300°C), the thermal regime influences the onset of clay dehydration reactions that generate fluid while developing new mechanical properties at the location of dehydration. Clay dehydration also facilitates buoyancy-driven fluid flow updip along permeable zones of the subduction thrust. Surface heat flow measurements provide a way to estimate the thermal regime of the margin and incoming slab. Surface heat flow is sensitive to subduction velocity and geometry, slab age, fluid discharge along faults and permeable zones, materials properties, and frictional heating.

Scientific interest in the Hikurangi subduction zone (Figure 1) has increased in recent decades due to the recognition of shallow slow slip events (SSEs) at this margin [*Douglas et al.*, 2005; *Wallace and Beavan*, 2006]. SSEs are characterized by fault motion lasting days to weeks or more, rather than seconds or minutes that are characteristic of earthquakes [*Schwartz and Rokosky*, 2007]. Continuous Global Positioning System (cGPS) and absolute pressure gauge (APG) data along the Hikurangi margin [*Douglas et al.*, 2005; *Wallace and Beavan*, 2006; *Wallace et al.*, 2004; *Wallace et al.*, 2012; *Wallace et al.*, 2016] has helped to establish the distribution of SSEs along strike and down dip. These measurements at the northern Hikurangi margin show that SSEs occur on average every 19 months in a patch extending from the Raukumara Peninsula to Hawke Bay, and within 100 km of the deformation front [*Wallace et al.*, 2016]. Here, SSEs yield a moment release equivalent to a M_w = ~7 earthquake [*Wallace and Beavan*, 2006; 2010]. Understanding the characteristics and physics of SSEs is important because they influence the local stress regime and moment release budget, and may influence the occurrence rate of great (M_w > 8.0) earthquakes. A

leading hypothesis contends that SSEs are modulated by excess fluid pressure [*Kitajima and Saffer*, 2012; *Kodaira et al.*, 2004; *Liu and Rice*, 2007]. At most margins SSEs are deep and thought to occur near the downdip transition between stick-slip and stable sliding behavior [*Dragert et al.*, 2001; *Hirose et al.*, 1999; *Obara et al.*, 2004]. In such an environment overpressures are thought to occur through the thermally controlled dehydration of hydrous minerals within the crust [*Kodaira et al.*, 2004; *Liu and Rice*, 2007]. In contrast SSEs along the northern Hikurangi margin are very shallow, with recent offshore deployment of APGs [*Wallace et al.*, 2016] establishing that slow slip events occur within ~ 2 km of the seafloor offshore Gisborne, New Zealand. In this environment over pressures may be driven by compaction of subducting sediments, low temperature dehydration of smectite, or a combination of both processes [*Bassett et al.*, 2014; *Ellis et al.*, 2015]. An important clue to understanding these processes and discriminating between them is the thermal regime.

Direct measurement of temperature at the location of shallow SSEs is not practical because drilling is time consuming, expensive and difficult. Instead temperatures are estimated through a combination of surface heat flow measurements and modeling. Heat flow data along the Hikurangi margin are relatively scarce and limited to landward of the deformation front. Existing data include downhole temperature measurements from exploration boreholes [*Field and Uruski*, 1997] and estimates from bottom simulating reflectors (BSRs) [*Henrys et al.*, 2003; *Townend*, 1997]. Heat flow values from 14 wells distributed along strike of the central and northern margin are generally between 40 and 80 mW m^{-2}, with a slight decrease in heat flow from north to south. Heat flow north of Hawke bay is generally between 50–80 mW m^{-2}, and south of Hawke Bay is 40–45 mW m^{-2} [*Field and Uruski*, 1997; *Henrys et al.*, 2003]. BSR estimates of heat flow along the continental slope of the Hikurangi margin show a landward decreasing trend in the heat flow consistent with its forearc setting and subduction of the Pacific plate. Heat flow values decrease from ~50 mW m^{-2} near

the deformation front to ~ 35 mW m^{-2} over a distance of 100 km [*Henrys et al.*, 2003].

The combination of these data have been used to make estimates of temperature along the plate boundary. McCaffrey et al. (2008) used a one-dimensional analytic model with a linear geotherm and estimated the 100°C isotherm to be at 10–15 km depth for the northern margin and 9–14 km depth for the southern margin. Fagereng and Ellis (2009) used a 2-D finite difference model with a linearly dipping slab, finding the 100°C isotherm occurring at a depth of 10 ± 2 km. The Fagereng and Ellis (2009) model also shows a sharp decrease in surface heat flow from 48 mW m^{-2} to 25 mW m^{-2} as the deformation front is crossed landward, then gradually increasing to 45 mW m^{-2} at 200 km landward of the deformation front. These heat flow values overlap the values of onshore wells south of Hawke Bay, but the higher heat flow values north of Hawke Bay (~80 mW m^{-2}) could not be replicated [*Field and Uruski*, 1997; *Henrys et al.*, 2003; *Townend*, 1997]. The confidence placed in these studies is limited because the relatively large uncertainties in converting BSR observations to heat flow and the generally poor knowledge of the thermal regime. These studies also relied on models requiring a straight plate interface when seismic reflection studies show the plate interface is more complex. Gao and Wang [2014] addressed this by developing a thermal subduction model of the northern Hikurangi with a more complex subduction geometry [*Ansell and Bannister*, 1996], giving a 100°C isotherm of ~7 km depth (42 km from deformation front).

In this study I report and analyze new heat flow measurements made across the northern Hikurangi margin. Heat flow observations have been corrected for the effects of bathymetry and sedimentation. To better understand the heat flow measurements across the margin I construct a two-dimensional advective-conductive heat flow model and explore its implications in terms of mineral dehydration reactions.

2. Tectonic Setting

The Hikurangi Trough lies at the southern end of the Tonga-Kermadec subduction zone and extends from offshore Raukumara Peninsula (northern North Island) to the southern Wairarapa coast and Cook Strait (Figure 1). The Hikurangi margin formed 20-25 Myr ago [*Ballance*, 1976; *Walcott*, 1987] in response to westward subduction of the thick and bathymetrically elevated Hikurangi Plateau, an early Cretaceous (120 Myr) large igneous province [*Davy and Wood*, 1994; *Davy et al.*, 2008; *Taylor*, 2006; *Wood and Davy*, 1994]. Subduction of the buoyant Hikurangi Plateau at ~3.5– 4.5 cm yr^{-1} [*DeMets et al.*, 2010] is a primary influence on shaping the Hikurangi subduction zone including the shallowness of the trench, the taper angle, and styles of deformation.

The Hikurangi Plateau is interpreted to be a remnant of the larger Ontong Java-Manihiki-Hikurangi (OJMH) large igneous province [*Davy et al.*, 2008; *Taylor*, 2006]. The OJMH appears to have been emplaced upon pre-existing oceanic lithosphere that was likely young and thin [*Kroenke et al.*, 2004]. Geochronological data ($^{40}Ar/^{39}Ar$) shows that the oldest of OJMH plateau-forming eruptions occurred as early as 125 Myr with samples clustering around 122 Myr [*Hoernle et al.*, 2010; *Tejada et al.*, 2002]. Mean basement $^{40}Ar/^{39}Ar$ ages indicate that Hikurangi Plateau volcanism began at least as early as 118 Myr. The Hikurangi also experienced more recent stages of volcanism at ages 98.7 ± 0.7 Myr to 87.5 ± 0.4 Myr, and 66.9 ± 6 Myr [*Hoernle et al.*, 2010]. Despite these younger eruptions, the bulk of OJMH plateau-forming eruption is thought to have occurred ≥ 117 Myr [*Hoernle et al.*, 2010]. The onset of breakup between the Hikurangi and the OJMH occurred along the Osbourne trough (Figure 1A) and is ≥ 115 Myr based on dacite ages from the West Wishbone Ridge [*Mortimer et al.*, 2006].

Although typical spreading-ridge generated crust is ~7 km thick, the Hikurangi Plateau has been thickened to approximately 12-15 km [*Davy and*

Wood, 1994; *Wood and Davy*, 1994]. With a depth of ~2600–5300 m below sea level [*Davy et al.*, 2008], the Hikurangi Plateau sits anomalously high compared to the depth range of ~4900–6100 m predicted by the GDH1 plate cooling model for lithosphere this age [*Stein and Stein*, 1992]

The Hikurangi Plateau is characterized by rough bathymetry studded with seamounts exposing extrusive volcanics to the ocean [*Wood and Davy*, 1994]. These seamounts are more numerous and larger in the northern Hikurangi Plateau than in the south and shape the northern Hikurangi margin by facilitating tectonic erosion of the forearc [*Collot et al.*, 1996; *Lewis et al.*, 1998]. The Poverty and Ruatoria embayments are examples where seamounts have deformed the forearc (Figure 1). Additionally, the bathymetric depressions of the rough basement facilitates subduction of sediment and pore-fluid [*Lewis et al.*, 1998]. This sediment is thought to underplate the North Island resulting in a net crustal growth [*Bassett et al.*, 2010; *Collot et al.*, 1996; *Lewis et al.*, 1998]. The subducting basement of the central and southern Hikurangi margin is generally smoother than the basement of the northern margin. In contrast to the north, the southern Hikurangi margin is characterized by tectonic accretion with lengthening of the forearc and imbricated splay faults [*Collot et al.*, 1996; *Lewis et al.*, 1998].

The erosive tectonic setting due to elevated and rough basement bathymetry and generally low sediment input leads to a steepened taper angle across the relatively short northern Hikurangi accretionary prism. The wedge taper angle is the combined angle between the basement dip (8– 5°) and the prism surface dip (> 3°), and is consistently > 10° in the northern Hikurangi. By comparison the longer accretionary prism (150 km) south of Hawke Bay has a lower wedge taper angle of 4° [*Fagereng*, 2011]. Generally, increased wedge taper is thought to be correlative with more efficacious fluid escape, lower pore fluid pressure, and higher effective shear stress and frictional heating than subduction margins with lower wedge taper angles.

Present-day sedimentation in the Hikurangi Trough is dominantly terrigenous and mainly sourced from the Kaikoura canyon (Figure 1) [*Lewis*, 1994; *Lewis and Pantin*, 2002; *Lewis et al.*, 1998]. Sediment is driven northward along the Hikurangi channel until rerouted eastward by outcropping seamounts and onto the Hikurangi Plateau [*Lewis et al.*, 1998], causing the Kermadec trench to be sediment starved and consequently deeper than the Hikurangi trough. Seaward of the Hikurangi Trough sediments have a thickness of > 1 km where not interrupted by basement topography. Sediment within the northern Hikurangi Trough is ~1 km thick and increases to ~6 km in the south [*Lewis et al.*, 1998; *Plaza-Faverola et al.*, 2012]. Underlying the terrigenous sediments across the Hikurangi margin are late Cretaceous to Oligocene nanofossil chalks and mudstones [*Davy et al.*, 2008] and Miocene pelagics [*Barnes et al.*, 2010; *Davy et al.*, 2008; *Plaza-Faverola et al.*, 2012].

Convergence of the Pacific plate is strongly oblique to the strike of the Hikurangi margin. In the northern margin, the difference in the azimuth between the Pacific plate velocity and trough-normal 05CM-04 seismic line is 33°. The northern study area has a total and trough-normal convergence of 44 and 37 mm yr^{-1} respectively. Convergence rate decreases southward, giving the southern study area a total and trench normal convergence of 37 and 30 mm yr^{-1} respectively [*DeMets et al.*, 2010].

A change in dip of the Wadati-Benioff zone suggests a termination of the Hikurangi Plateau ~37–140 km beneath the North Island and northern end of the South Island of New Zealand [*Reyners et al.*, 2011]. Thus the Hikurangi Plateau is unique as possibly the only known large igneous province currently undergoing subduction.

3. Heat Flow Measurements

Marine heat flow measurements presented in this study were collected from May 20–June 15 2015 onboard the *R/V Roger Revelle*, cruise RR1508, and from 19–30 June 2016 onboard the *R/V Tangaroa*, cruise TAN1607. A total of 96 measurements were collected across the northern Hikurangi margin and are collocated along seismic reflection lines TAN1114-01, TAN1114-24, and 05CM-04 (Figure 2).

Heat flow data were acquired using a 3.5 m long violin-bow style probe [*Hyndman et al.*, 1979]. The heat flow probe consists of a weight stand containing a data logger, pressure sensor and acoustic transducer (Figure 3). The acoustic transducer sends data through the water to the surface so that probe performance can be monitored in real time. The 3.5 m lance supports a string of 11 temperature sensors within a protective housing. This design provides both the mechanical robustness to withstand repeated insertions-withdrawals from the sediment and sensitivity needed to make highly accurate measurements. Internal power allows 20–24 measurements during a single lowering of the probe, with profiles lasting as long as 48 hours depending on power use for *in-situ* thermal conductivity determination.

Each heat flow measurement (Figure 4) starts by holding the probe 100-200 m above bottom to collect bottom water temperatures. After this time period the probe is lowered into the sediment at a rate of 60 m minute^{-1}. Temperatures measured by each temperature sensor initially increase due to frictional heating caused by penetration of the probe. With time these temperatures decay toward equilibrium values within the sediment. Although the temperatures do not reach equilibrium, a time series of seven minutes is used to extrapolate to an equilibrium temperature. Extrapolations are computed by comparing the observed temperature sensor response to a mathematical representation of radial heat conduction from a line source [*Carslaw and Jaeger*, 1959]. Once

equilibrium temperatures are estimated the thermal gradient is computed using knowledge of the thermistor spacing along the string.

In-situ thermal conductivity is calculated by monitoring the thermal decay of a calibrated heat pulse generated by heating elements within the temperature sensor housing. The thermal conductivity is proportional to the decay of the calibrated pulse. The mathematical details of each step are given in [*Villinger and Davis*, 1987], and [*Hartmann and Villinger*, 2002].

In practice, non-linear inversion techniques are used to calculate solutions of equilibrium temperature based on frictional heating decay, and thermal conductivity at each temperature sensor depth based on active heat pulse decay [*Hartmann and Villinger*, 2002]. The conductive heat flow through the seafloor is calculated using summed thermal resistance [*Bullard*, 1939],

$$T(z) = T_o + q_o \sum_{i=1}^{N} \frac{\Delta z_i}{k(z)_i}, \qquad (1)$$

Where T_o is the equilibrium temperature at depth, z, q_o is the observed heat flux, $k(z)$ is the thermal conductivity measurement over the i^{th} depth interval Δz_i, and the summation is preformed over N depth intervals from the surface to the depth of interest z. In practice q_o and T_o are estimated by plotting against summed thermal resistance $\Sigma(\Delta z_i / k(z)_i)$.

3.1 Heat Flow Corrections

Observed temperature gradients from the northern Hikurangi field site are the superposition of the background geothermal gradient with gradients introduced from environmental factors including, sedimentation, bathymetry, and bottom water temperature fluctuations. I calculate a corrected temperature gradient by quantifying and removing the environmental factors from the observed gradient.

3.2 Bathymetric Corrections

Variations in bathymetry can distort the shallow thermal regime. Under bathymetric highs and lows the vertical temperature gradient decreases and increases, respectively, relative to background conditions. I correct for the effects of bathymetry using a 3-D finite difference algorithm [*Phrampus*, written comm., 2016] solving for surface heat flow. Bathymetry is estimated using a digital elevation model for the Hikurangi region and is coupled with conductivity, temperature, and depth (CTD) casts [*Harris et al.*, 2015] to estimate seafloor temperatures. I assume a constant basal heat flux and steady state conditions. Corrections account for the effect of bathymetry in an area 1 km^2 around the heat flow measurement. The minimum and maximum bathymetric correction applied are +19% and -56% respectively.

3.3 Sedimentation Correction

The rapid deposition of sediment at bottom water temperature can transiently decrease the observed thermal gradient relative to background until the sediment warms to ambient conditions. The magnitude of this effect depends on the rate and duration of sediment accumulation and is most sensitive to the last large sediment accumulation event e.g.[*Powell et al.*, 1988].

At the Hikurangi margin and trough, the primary data for estimating the magnitude of sedimentation perturbations are seismic reflection records that provide estimates of sediment thickness, and short sediment cores that provide sediment accumulation rates to as far back as the Kawakawa tephra, 22,590 yr b.p. [*Carter et al.*, 1995]. Heat flow measurements are collocated with seismic reflection records so that sediment thickness can be estimated. To convert two-way travel times to sediment thickness, I use a stratigraphic interpretation [*Davy et al.*, 2008; *Henrys et al.*, 2013; *Pedley et al.*, 2010; *Plaza-Faverola et al.*, 2012] and a fit to the local velocity analysis model from [*Ellis et al.*, 2015],

$$d = -0.00396 + 0.788t + 0.257t^2 - 0.0112t^3, \quad (2)$$

where d is sediment thickness in meters, and t is two-way time in seconds.

Sediment cores along the Hikurangi margin (Figure 5) are relatively well distributed but cores from the Hikurangi Plateau are relatively sparse [*Carter et al.*, 1995; *Collot et al.*, 2001; *Lewis and Kohn*, 1973; *Pouderoux et al.*, 2012]. A limitation of these cores is that each is only several meters in length, restricting our knowledge of the accumulation history to the recent past, but the combination of these cores is revealing of Hikurangi Plateau sedimentation history. Mean and one standard deviation values of cores seaward of the Hikurangi Trough are 0.078 ± 0.054 mm yr^{-1}, while values on the margin are 0.28 ± 0.27, showing that sediment accumulation rates seaward of the Hikurangi trough are much lower and more consistent than those on the margin. The lower accumulation rates are consistent with their pelagic and hemipelagic setting. Landward of the deformation front accumulation rates are more heterogeneous reflecting the heterogeneity of sediment flow paths, deposition, and erosion.

The sedimentation correction for heat flow measurements seaward and landward of the deformation are discussed separately. Figure 6 displays the generalized sediment accumulation history seaward of the deformation front. Basement consists of the 120 Myr Hikurangi Plateau and is overlain by pelagic and hemipelagic sediments reflecting the deep sea environment of the seafloor for times between ~120 Myr to 5 Myr. Sediment accumulation rates for this interval are low at 5.26×10^{-6} m yr^{-1}. Between 5 Myr and 170 kyr, the pre-Ruatoria unit is deposited and the accumulation rate increases to 7.25×10^{-5} m yr^{-1} as terrigenous sediments become dominant [*Lewis et al.*, 1998]. The Ruatoria Avalanche dated at 170 ± 40 kyr [*Collot et al.*, 2001] caused the dispersal of a seismically transparent and regionally extensive debris flow that provides a good marker bed. Sediments deposited between 170 kyr and the present are referred to as the post-Ruatoria unit and have an accumulation rate of 9.71×10^{-4} m yr^{-1}.

I compute the thermal impact of sediment accumulation using SlugSed, a 1-D finite difference numerical algorithm [*Hutnak and Fisher*, 2007] that models lithospheric cooling with the effects of multiple sediment accumulation stages, and compaction. SlugSed uses a deforming grid, with new elements added as accumulation proceeds. The influence that each sediment accumulation stage has on the surface heat flow can thus be tested and informs our regional heat flow correction for sedimentation. The material parameters used with SlugSed are given in Table 1. GDH1 plate cooling parameters [*Stein and Stein*, 1992] are used for initial temperature distribution, thermal diffusivity, heat capacity, and slab thickness. The SlugSed model allows a user-defined porosity-depth relation defined by Athy's law,

$$\varphi(z) = \varphi_0 \, exp(-hz), \tag{3}$$

where φ is porosity as a function of depth, z, φ_0 is the initial porosity and h is an empirical compaction constant. Because of a lack of information about sediment compaction on the Hikurangi Plateau we use parameter values of φ_0 = 0.7, h = -8.334 $\times 10^{-4}$ m, from *Davis et al.* [1999]. There values are in general agreement with those derived from ODP Sites 1123c (φ_0 = 0.72, h = -1.023 $\times 10^{-3}$ m^{-1}) and 1124c (φ_0 = 0.77, h = -9.99 $\times 10^{-4}$ m^{-1} [*Shipboard Scientific Party*, 1999a; b] seaward of the Hikurangi Margin.

Results of my preferred sedimentation model are given in Table 2 as a function of each sediment accumulation stage. The Ruatoria Avalanche is modeled as an instantaneous accumulation event. The total correction increases the heat flow by 21%. The post- and pre-Ruatoria turbidites have the largest impact accounting for 10 and 6% of the total correction, whereas the Ruatoria avalanche and pelagic unit account for only 3 and 2% respectively.

To understand uncertainties in the sedimentation model, I adjust the sediment accumulation rates and bed thickness for high and low sedimentation end member

scenarios of the pre-Ruatoria unit, Ruatoria Avalanche, and post-Ruatoria unit. End member accumulation rates and thicknesses are based on the variability in bed thicknesses observed in seismic data. Variability in accumulation rate of the pelagic unit has little effect on the sedimentation correction and so it is not altered in this sensitivity study. The results are summarized in Table 2. The high sedimentation correction model results in thicker units because sedimentation rate has been increased while the deposition times have been fixed. An increase in sedimentation rate between the pre and post-Ruatoria units and a thicker Rautoria Avalanche leads to an increase in the correction to about 26%. The low sedimentation correction model results from thinner units that decrease the sedimentation rate. In this scenario we remove the Ruatoria Avalanche and reduce the sedimentation rate of the pre and post Ruatoria units, leading to sediment correction of 14%. This analysis indicates that the sedimentation correction is 21% with an uncertainty ~7%. The sedimentation models including the Ruatoria Avalanche show that it is responsible for a reduction of surface heat flow by 3–4%. It has a less significant role in influencing present day surface heat flow than either of the adjacent units because it is relatively thin. A scenario in which the thicknesses of the post-Ruatoria unit and the Ruatoria Avalanche are combined into a single unit immediately seaward of the deformation front along seismic line 05CM-04 is shown in *Pedley et al.* [2010]. This scenario leads to a sediment correction of 22% that falls within our uncertainty.

For measurements landward of the deformation front I use the sedimentation correction of 20% based on an average sedimentation rate of 0.4 mm yr^{-1} for the period from 5 Myr to present [*Townend*, 1997]. A standard deviation of ± 0.1 mm yr^{-1} is used to account for variability in sedimentation across the Hikurangi margin [*Henrys et al.*, 2003; *Townend*, 1997].

3.4 Bottom Water Temperature Variations

Fluctuations of bottom water temperature (BWT) can have a temporal influence on the shallow sub-seafloor geotherm. Approximately one-year prior to our heat flow measurements, absolute pressure gauges (APG) and ocean bottom seismometers (OBS) were deployed throughout the northern study area as part of the HOBITSS experiment [*Wallace et al.*, 2016]. Temperature loggers were deployed with these instruments during cruise TAN1405 in May 2014 and recovered on cruise RR1509 in June 2015. Analysis of these temperature-time series show that the influence of BWT fluctuations diminish with seafloor depth and are negligible at the depth of the heat flow measurements (Appendix). Thus, no corrections are applied for BWT variations.

3.5 Heat Flow Data

In the northern field area heat flow data was collected along four transects (Figure 2). One transect was collected as far east as feasible to estimate the background thermal state of the Hikurangi Plateau. Two transects were collected to test for the presence of advective fluid flow associated with the Tūranganui Knolls, and two transects crossed the deformation front. All heat flow measurements are collocated with seismic reflection profiles and swath bathymetry to provide information about the local measuring environment and our measurement spacing is nominally 400 m but decreases over targets of interest such as buried basement relief and faults. Closely spaced heat flow measurements are a precaution against aliasing the data.

The transect to estimate background values of heat flow is located along seismic line TAN1114-01 and is the most seaward set of values collected (Figure 2). Eight measurements were made along this transect (Figure 7). Corrections for bathymetry are negligible and given its distal location the sediment correction may be over-estimated. Corrected heat flow values vary systematically between 45 and 71 mW m^{-2}. The GDH1 plate cooling model for oceanic lithosphere (Stein

and Stein, 1992) with an age of 120 Myr predict a value of 53 mW m^{-2} and an uncertainty of ± 10 mW m^{-2} due to uncertainties in model parameters. The 56 mW m^{-2} mean of these values is consistent with GDH1 model predictions for 120 Myr lithosphere. However, variability in heat flow is greater than the expected range and the source of this variability is unclear. Locally there is a lack of bathymetry, but just to the south fluid flow associated with a seamount may be causing the perturbations.

Heat flow transects to test for advective fluid flow associated with the Tūranganui Knoll are shown in Figure 8. Both transects are along seismic line 05CM-04. One transect consisting of four measurements between CDP values of 7300 and 7400 are located near a small pinnacle on the Tūranganui Knoll. Because of the thin sediment cover no correction for sedimentation is made to these values. Surprisingly, the bathymetric correction is relatively small. Heat flow values here vary between 65 and 82 mW m^{-2}, and are above the GDH1 prediction and mean of the equilibrium transect values. Without more contextual information the magnitude of these values are inconclusive but consistent with fluid discharge. The second heat flow transect lies between CDP values of 5800 and 6500 adjacent to the Tūranganui Knoll (Figure 8). Adjacent to the Knoll heat flow is as low as ~ 28 mW m^{-2} and then increases steadily to a relatively uniform value of ~ 62 mW m^{-2} about 3 km landward of the Knoll. This pattern of heat flow is consistent with fluid recharge through exposed basement near the sediment-basement interface at CDP 6510. The combination of the mean of values along the equilibrium transect and the uniform values distal of the Tūranganui Knoll suggest a background heat flow value of 59 mW m^{-2}.

We collected heat flow transects across the deformation front along seismic lines TAN1114-24 (Figure 9) and 05CM-04 (Figure 10). Seaward of the deformation front, both seismic reflection profiles show buried seamounts or a basement ridge. We test for the presence of fluid flow in the basement by

measuring heat flow over these features. Along seismic line TAN1114-24 and seaward of the deformation front, heat flow has a mean value of 62 mW m^{-2} and varies between 39 and 103 mW m^{-2} (Figure 9). Along seismic line 05CM-04 and seaward of the deformation front heat flow has a mean value of 62 mW m^{-2} and varies between 45 and 83 mW m^{-2}. Heat flow values along both lines appear to inversely correlated with sediment thickness and this relationship is explored in the next section.

The heat flow transect along seismic line TAN1114-24 only extends about 5 km landward of the deformation front and crosses the first anticlinal ridge (Figure 9). Heat flow values at CDP 22186 and 22326 show relatively high values and although these higher values are consistent with fluid discharge not enough is known to confidently ascribe the anomalies to a particular cause. Heat flow is relatively constant over the anticlinal ridge with a value of 44 mW m^{-2}. Heat flow measurements along seismic line 05CM-4 landward of the deformation front show several interesting patterns (Figure 10). Heat flow values vary between 22 and 63 mW m^{-2}. Although heat flow generally decreases landward there is a sharp discontinuity in heat flow of approximately 40 mW m^{-2} near CDP 4300.

In total, the mean of all northern Hikurangi Trough heat flow measurements seaward and landward of the deformation front is 58 and 46 mW m^{-2} respectively. These values indicate a landward decreasing trend in heat flow consistent with the forearc setting. Mean values of heat flow seaward of the deformation front are slightly higher than predicted by GDH1 [*Stein and Stein*, 1992] but within the range of uncertainty.

3.6 Evidence for Advective Fluid Flow in the Basement

In ridge flank settings where the crust is young and permeable an inverse correlation between heat flow and sediment thickness is observed and interpreted as evidence for fluid flow to maintain approximate isothermality along the sediment basement interface [e.g., *Davis et al.*, 1989, 2004]. A similar

phenomenon is also seen at the 106 Myr Madeira Abyssal Plain [*Fisher and Von Herzen*, 2005], far beyond the 65 Myr "sealing age" [*Stein and Stein*, 1994]. To test for fluid flow within the basement structure just seaward of the deformation front along line TAN1114-24, I explore the degree of basement isothermality implied by our data as informed by the inverse relationship between heat flow and sediment thickness. The inverse relationship between sediment thickness and heat flow can be described by,

$$q_{obs} = K_m \frac{T_{interface} - T_s}{\Delta z}, \quad (4)$$

where q_{obs} is the observed heat flow, K_m is the harmonic mean thermal conductivity of the sediment bed with thickness Δz, $T_{interface}$ is temperature at the sediment-basement interface, and T_s is seafloor temperature. The dashed lines in Figure 11 shows this relationship for various isothermal temperatures of the sediment-basement interface.

Sediment thickness is estimated from two-way travel time using Equation (2) and varies between 300 and 1150 m. The mean thermal conductivity is estimated using Athy's Law (Equation 3) and the parameters presented by *Davis et al.* [1999] ($\varphi_0 = 0.7$, $h = -8.334 \times 10^{-4}$ m) to estimate porosity with depth, and the grain thermal conductivity of the sediment. Grain conductivity is calculated using the thermal conductivity of water and mean probe thermal conductivity measurements (1.0 W m^{-1} K^{-1}) according to the geometric mean,

$$K_G = \left(\frac{K}{K_w{}^{\phi}}\right)^{1/(1-\phi)}, \quad (5)$$

Where K_G is grain thermal conductivity, K is the probe thermal conductivity of the sediment, K_w is the thermal conductivity of water (0.6 W m^{-1} K^{-1}), and ϕ is porosity at depth. Thermal conductivity for each depth is calculated according to,

$$K(z) = K_w{}^{\phi(z)} K_G{}^{1-\phi(z)}, \quad (6)$$

where K(z) is thermal conductivity at depth z, and $\phi(z)$ is porosity at depth z. This relationship accounts for porosity loss through compaction with depth. Mean values of thermal conductivity vary between 1.14 and 1.51 W m^{-1} K^{-1}. I find that this model predicts temperatures at the sediment-basement interface to ± 5° for the ridge imaged along line TAN1114-24. There is some systematic misfit that is likely due to non-isothermality along the sediment-basement interface, but may also be influenced by the application of the sediment correction, or heat refraction effects. Comparing the heat flow data from the 05CM-04 line to 1-D isothermal basement model predicts a sediment-basement temperature to ± 10°C, with slightly more scatter about the mean modeled isotherm.

5. Thermal Model

To better understand heat flow variations and the thermal regime landward of the deformation front I construct a two-dimensional finite element model using the algorithm constructed and described by *Wang et al.* [1995]. This algorithm solves the heat conduction-advection equation described by,

$$\nabla(K\nabla T) - cpv\nabla T + A = 0, \qquad (7)$$

where K is thermal conductivity, T is temperature, cp is volumetric heat capacity, v is convergence rate of the subduction slab, and A is heat generation. Heat is transferred advectively with the subducting material based on a convergence rate of 37 mm yr^{-1}, and is transferred conductively through the accretionary prism, upper crust, and lower crust. The mantle wedge is coupled to the subducting plate and is modeled using an isoviscous mantle rheology[*Peacock and Wang*, 1999]. The details of the mantle rheology have only a small effect on the shallow portion of the subduction thrust, the focus of this study.

The 2-D thermal model is positioned along seismic line 05CM-04 that is approximately trough-normal (Figure 10). The geometry of the shallow subduction thrust between the deformation front and the 50 km landward is guided by seismic reflection data from the 05CM-04 and 05CM-05 lines [*Bell et al.*, 2010]. Between this distance and the Taupo Volcanic Zone the plate interface is based on relocated earthquake hypocenters [*Williams et al.*, 2013]. Landward of the Taupo Volcanic Zone (~220 km from deformation front), the subduction thrust is assigned a constant in slope of 43°. Bathymetry and topography data defining the margin and sub-aerial region of the transect comes from the GeoMapApp Global Multi-Resolution Topography (GMRT) synthesis [*Ryan et al.*, 2009].

The thermal model is divided into six thermal physical units (Figure 12). Each thermal unit of the model uses homogeneous thermophysical parameters (Table 3). Sediment parameter values are based on other studies [*Currie et al.*, 2002; *Ellis et al.*, 2015; *Harris et al.*, 2010; *Hyndman and Wang*, 1993; *Oleskevich et al.*, 1999]. I assume that the Hikurangi Plateau has thermophysical properties similar to that of oceanic crust. The accretionary prism, consisting of mudstone, sandstone, siltstone, and carbonates, extends from the deformation front to 170 km landward where transition occurs to the indurated Late Cretaceous indurated sediments of the Matawai Group in the Raukumara ranges. The bulk of sediment deposited in the northern Hikurangi Trough is subducted, and seaward of the deformation front we use a constant thickness of 1200 m for the sediments. Basement roughness and underplated sediments are not included in the model. The overriding plate has a crustal thickness of 35 km [*Reyners et al.*, 2011] and is divided into upper and lower crustal units at a depth of 25 km.

The model extends between 10 km seaward of the deformation front and 300 km landward of the deformation front. The landward and bottom sides of the model are sufficiently far so that the boundary conditions have a negligible effect

on the forearc region. The model uses a 1 km horizontal grid spacing between the seaward extent of the model and 30 km landward of the deformation front. Landward of 30 km from the deformation front a 5 km grid spacing is used. All boundary conditions of the model use fixed temperatures. The seaward boundary condition of the model is defined by the geotherm of the incoming oceanic lithosphere that is appropriate for 120-Myr old cooling lithosphere using parameters from GDH1 [*Stein and Stein*, 1992]. A basal temperature of 1450°C and a lithosphere thickness of 80 km are used, and give a lithosphere with surface heat flow matching the mean of all measurements seaward of the deformation front (58 mW m^{-2}) in this study. The landward boundary condition through the continental crust is defined by a conductive geotherm with heat generation resulting in a surface heat flow of 80 mW m^{-2}, common to backarc settings [*Currie and Hyndman*, 2006]. The geotherm through the mantle wedge follows an adiabatic gradient of 0.4°C km^{-1}. The surface boundary condition is set to 1°C seaward of the deformation front based on CTD cast data [*Harris et al.*, 2015] and 15°C for sub-aerial locations. The surface temperature of the margin increases from 1° to 15°C following the temperature-depth relationship of CTD cast data.

Heat generated from friction along the plate interface fault can produce a significant increase in surface heat flow [*Wang et al.*, 1995]. Frictional heat generation, Q_f, within the shear zone along the subduction thrust fault can be quantified in the brittle regime as,

$$Q_f = \tau v = \mu' \sigma_n v = \mu(1-\lambda)\sigma_n v, \quad (8)$$

Where τ is shear stress, v is velocity across the shear zone, μ' is effective coefficient of friction, σ_n is normal stress, and μ is coefficient of friction. The pore fluid ratio is defined as,

$$\lambda = (p_f - p_d)/(p_l - p_d), \quad (9)$$

Where p_f, p_d, and p_l are respectively fluid pressure, pressure at surface, and lithostatic pressure [*Byerlee*, 1978; *Wang et al.*, 1995]. Overpressuring to near lithostatic pressures results in λ values approaching 1, while hydrostatic conditions result in λ values of ~0.4. The sliding velocity is set to 38 mm yr^{-1} based on the MORVEL-derived convergence velocity and obliquity between the Australian and Pacific plate [*DeMets et al.*, 2010]. Gao and Wang [2014] have used μ' values of 0.025–0.18 to satisfy thermal subduction models of the northern Hikurangi subduction zone.

In the ductile regime, frictional heating is generated per unit volume according to,

$$Q_f = \tau\dot{\varepsilon}, \tag{10}$$

where $\dot{\varepsilon}$ is the strain rate determined by the flow law of diabase, which is assumed to control the rheology of the ductile regime [*Caristan*, 1982]. The serpentinized mantle below the continental Moho of 35 km is assumed to be too weak to generate frictional heating [*Currie et al.*, 2002].

The preferred model is characterized by an incoming slab with heat flow of 58 mW m^{-2}, in agreement with the mean of heat flow values seaward of the deformation front acquired in this study. The model heat flow then decreases rapidly within just 2 km landward of the deformation front, a pattern that is also seen in the data as a decrease in measured heat flow along line 05CM-04 from 58 to ~ 40 mW m^{-2} at 2 km of the deformation front. In the model there is a local increase in heat flow by ~7 mW m^{-2} at 15 – 50 km from the deformation front that exists over an otherwise gradual landward increase toward continental backarc values.

Landward of 2 km from the deformation front, the heat flow data does not decrease with the consistency apparent in the model, and instead remains relatively elevated with local depressions at CDP4009 and ~4300. The data mean

value is 44 mW m^{-2} landward of the deformation front, with a landward decreasing trend of 2.2 mW m^{-2} km^{-1}. The maximum values landward of the deformation front are not duplicated by the model, but the lowest heat flow values landward of the deformation front (~25 mW) are nearest to heat flow models having $\mu' = 0$ to 0.03. From 80–180 km landward of the deformation front, the borehole heat flow data of Field [1997] and Pandey [1981] have the best RMS fit with μ' values of 0.18 and 0.13 respectively.

6. Parameter Sensitivity

A primary goal of the thermal model is to estimate temperatures along the subduction thrust. These temperatures are model dependent and it is instructive to examine the sensitivity of calculated isotherm positions to assumed parameter values. I explore the sensitivity of subduction thrust temperature to plate convergence velocity, subduction interface geometry, the seaward geotherm, and frictional heating. Plate convergence velocity and the geometry of the subduction interface control the rate of advective heat transfer as the incoming slab descends downdip. The geotherm is largely a function of the lithospheric age. The coefficient of friction influences the heat generated along the subduction thrust. I track the position of the 100° and 150°C isotherms in this sensitivity analysis because they are thought to play a key role in controlling the position of fluid generation through clay mineral dehydration [*Moore and Saffer*, 2001]. The 350°C isotherm has been suggested as controlling the downdip limit of seismicity and is also tracked in the sensitivity analysis. In the sensitivity analysis I vary each model parameter from its preferred value across a range of values. A summary of parameter sensitivity is given in Table 4.

One of the better known parameters is the long-term convergence rate. Uncertainties in angular velocity between the Pacific and Australian plate pair are small [*DeMets et al.*, 2010], propagating to less than ± 2.5% uncertainty in linear

convergence velocity at the Hikurangi margin. Variations in the convergence rate lead to small shifts in key isotherms of less than 1 km (Table 4).

The geometry of the plate interface is estimated from seismic reflection profiles at shallow depths and Wadati-Benioff earthquakes at depth. Uncertainty in seismic velocity leads to uncertainties in the position of the plate interface. The plate interface along seismic line 05CM-04 has a notable bend at ~37 km landward of the deformation front [*Barker et al.*, 2009; *Bell et al.*, 2010] and depth uncertainties increase with greater depth [*Barker et al.*, 2009]. The sensitivity of temperatures along the subduction interface are tested by adjusting the dip landward of 37 km from the deformation front by ± 5°. An increasing plate dip warms the plate interface and shifts the 150° and 350°C isotherms seaward. The 100°C isotherm is seaward of the change in dip and does not move. Conversely a decrease in plate dip cools the plate interface shifting the 150° and 350°C isotherms landward. Because the change in plate interface increases with distance from its hinge point the change in the 350°C isotherm is most dramatic at tens of kilometers.

Oceanic geotherms are commonly parameterized as a function of crustal age. The preferred model uses a crustal age of 120 Myr that results in a surface heat flow of 58 mW m^{-2} for the incoming plate. Variations in age by -10% and +20% are somewhat larger than the reasonable range of ages for the Hikurangi Plateau. These variations in the geotherm yield surface heat flow values for the incoming plate of 57.4 and 58.6 mW m^{-2}, respectively. The effect on surface heat flow landward of the deformation front is < ± 0.3 mW m^{-2}. In these tests sedimentation rates are adjusted so that they have the same thermal impact on the surface heat flow. Table 4 shows that reducing the lithospheric age to 108 Myr (10%) warms the subduction thrust and moves the isotherms toward the deformation front. Conversely, increasing the crustal age to 144 Myr cools the subduction thrust causing the isotherms to move deeper in the system. The net change in the

position of these isotherms is less than 1 km. The reason for the lack of sensitivity to the seaward geotherm is because old oceanic crust is near thermal equilibrium.

Perhaps the least constrained parameter is the effective coefficient of friction. Relative to Byerlee's law that finds a coefficient of friction of 0.6 for rocks in laboratory studies, results of field experiments find a much lower value for the coefficient of friction e.g.[*Fulton et al.*, 2013; *Gao and Wang*, 2014; *Lachenbruch and Sass*, 1980]. I explored the sensitivity of subduction thrust temperatures and surface heat flow to variations in the quantity of frictional heating along the subduction thrust. I find that variations in frictional heating parameter significantly affect the thermal regime. These findings are noted by other authors [*Gao and Wang*, 2014; *Hass and Harris*, 2016]. Using the full shear velocity of μ' = 44 mm yr^{-1} and a value of μ' = 0.13 as reference, I find that increasing μ' to 0.18 shifts the 100°, 150°, and 350°C isotherm seaward by 3, 13, and 13 km respectively. Decreasing μ' to 0.08 shifts the 100°, 150°, and 350°C isotherm seaward by 9, 10, and 21 km respectively. Adjusting the shear velocity to μ' = 38 mm yr^{-1} to accommodate for slip along the North Island dextral fault system, frictional heating shifts the 100°, 150°, and 350°C isotherms seaward by 2, 3, and 5 km respectively compared to the full convergence velocity of 44 mm yr^{-1}. Frictional heating is not modelled along the North Island dextral fault system.

7. Discussion

Heat flow data associated with the Tūranganui Knoll and incoming basement relief shows evidence for the presence of thermally driven fluid flow (Figures 8, 9, and 10). Conductive heat transfer cannot explain the data because heat refraction would produce higher heat flow in the locality of the thinning sediment, contrary to observation. At the Tūranganui Knoll, the low heat flow of sediment abutting the exposed basement is likely due to recharging fluids, and the higher than average heat flow associated with the pinnacle indicates discharging fluids.

These observations are consistent with numerical models showing that fluid discharge and recharge occurs at exposed basement [*Harris et al.*, 2004]. Although it is tempting to infer a connection between the recharging and discharging areas in this knoll, it is not demanded by the data, and several interacting flow loops may be present. Heat flow anomalies relative to GDH1 appear to be locally significant rather than regionally significant. The mean of the heat flow measurements associated with the Tūranganui Knoll is 55 mW m^{-2} close to the GDH1 predicted value. Computing a mean in this way does not constitute a quantitative heat budget but does indicate that the heat flow anomalies reflect a local redistribution of heat.

This finding of advective fluid flow is significant. Global heat flow data shows that hydrothermal circulation associated with ridge flanks plays an important role in advecting heat from the lithosphere until ~65 Myr [*Stein and Stein*, 1994], at which time the global average heat flow anomaly approaches zero. The consistency between heat flow data and plate cooling models for crust older than ~65 Myr is taken as evidence that advective fluid flow largely ceases and this age is often referred to as the 'sealing age'. This conventional wisdom has been challenged by the 106 Myr Madeira Abyssal Plain [*Fisher and Von Herzen*, 2005] where it has been found that variations in heat flow of ±10–20% from the mean value correlate inversely with sediment thickness. They find that fluid flow can explain the reduction of temperature difference between peaks and troughs along the sediment-basement interface, and suggest an upper crustal permeability of 10^{-12} to 10^{-10} m^2 based on a fully coupled heat and fluid flow models. Compared to the Madeira Abyssal Plain data, the sediment-basement interface in the northern Hikurangi more closely approaches isothermality as indicated by the heat flow data presented in this study. My results indicate a difference of ± 5° C across the sediment-basement interface along line TAN1114-24, while the Madeira Abyssal Plain data indicates a temperature difference of ± 15° C across the sediment-basement interface. This makes the degree of isothermality in this study more

comparable to observations at the much younger Juan de Fuca Ridge, where temperature differences also approach isothermal to within ± 5° C along the sediment basement interface of a buried ridge [*Davis et al.*, 1997]. Together these studies suggest that the permeability of oceanic crust can remain high and that fluid flow can remain active in old oceanic crust. It may be that the style of hydrothermal circulation gradually changes from being regionally significant on young crust to locally significant on old crust.

Landward of the deformation front, the surface pattern of heat flow is controlled by the subduction of the Hikurangi Plateau and dynamics of the margin. Heat flow landward of the deformation front (Figure 10) shows a complicated pattern of ups and downs. Just landward of the deformation front, heat flow drops but then increases over the first anticlinal ridge before showing a linear decrease to values of approximately 20 mW m^{-2}. At CDP 4300 heat flow suddenly jumps to a value of about 60 mW m^{-2} before declining to a value of 20 mW m^{-2} at CDP 4009. Landward of this minima heat flow increases to about 40 mW m^{-2}.

The observed variations and offset in heat flow is enigmatic, but the sharpness of the offset suggests a shallow source. One candidate source that might cause the observed variations is slumping. A slump deposit is identified with seismic data between CDP 4200 and 4375. The slump headwall exposes previously buried sediment and leads to an increase in heat flow. The heat flow signature on the slumped block is less certain but if it remains intact the heat flow would stay approximately the same. This pattern correlates qualitatively with the heat flow data, but the mapped slump straddles the heat flow offset such that the upper part of the slump deposit is associated with high heat flow values and the lower part is associated with low heat flow values (Figure 10). It is difficult to reconcile the position of the slump deposit with the heat flow offset, but alignment between them cannot yet be ruled out because complex 3-D bathymetry at this location is

very complex and the lateral resolution of the 05CM-04 line is significant compared to the scale of the bathymetry.

A second candidate source is fluid flow. Between CDP values of 4375 and 4450 a series of splay faults intersect the surface. The trend of seaward increasing heat flow may be due to the geometry of the faults and warm fluids egressing through them. With this explanation the heat flow offset seen at CDP 4300 would correspond to the intersection of a splay fault with the seafloor. There are several candidate splay faults interpreted seismically in this region but limits on image resolution and out-of-plane effects make correlation difficult. High resolution bathymetry data (25 m) however shows a daylighting fault cross cutting the deformation front directly across the slump, making it a likely candidate for fluid discharge.

Figure 13a compares thermal model results as a function of the effective coefficient of friction with the heat flow data. For the effective coefficient of friction, I test a range from 0 to 0.18 based on values from other studies [*Fagereng and Ellis*, 2009; *Gao and Wang*, 2014; *McCaffrey et al.*, 2008]. In general, both the model and the data show a decline in heat flow landward of the deformation front. However, the model shows a more abrupt and steeper decline than the data. Given that heat flow landward of the deformation front is generally in excess of values predicted by the conducive model used in this study, and that the model does not duplicate the heat flow data structures seen across CDP 4000–4500 along line 05CM-04, I consider it likely that heat transfer is occurring advectively as fluid flow through a fault system to maintain heat flow above the expected modeled values of ~25–40 mW m^{-2}. I conclude that the heat flow increase landward of CDP 4009 is caused by fluid discharge along an interpreted splay fault, leaving the heat flow depression at CDP 4009 as the region least thermally affected by fluid discharge and the most representative of the conductive heat transfer regime near the deformation front. Using these low

values of heat flow as a guide suggests that the effective coefficient of friction along the subduction thrust fault within ~11 km of the deformation front is 0.03 or smaller.

Figure 13a also compares a number of other thermal models to the heat flow data. The model of Henrys et al. [2003] is constrained with heat flow estimated from BSRs. Their model shows a constant decrease in heat flow that does not capture the complexity of this margin. The models of Fagereng et al. [2009] use μ' values of = 0.03 to 0.36 to test the range of likely high and low pore fluid pressure scenarios, respectively. The high pore fluid pressure model ($\mu' = 0.03$) is most consistent with the heat flow data. Gao and Wang [2014] use μ' values of 0.03 to 0.13 and consider use $\mu' = 0.13$ to be an optimal fit based on data landward of our model. Finally, Ellis et al. [2015] explore the effects of a deforming margin due to the subduction of a seamount. This thermomechanical model incorporates a pressure sensitive rheology and computes fluid release from compaction and dehydration as a function of porosity, pressure and temperature, but does not include friction heating along the subduction thrust. The agreement between this model and data suggests that the impact of a deforming margin and fluid release and flow are important components to the thermal regime of this margin.

Identifying a source of fluid is important towards supporting the suggestion that fluid flow is responsible for elevated heat flow landward of the deformation front. Commonly considered fluid sources in the northern Hikurangi margin are from compaction of subducted sediment, and clay dehydration. Fluid release from compaction occurs nearly immediately downdip of the deformation front and increases by a factor of 6 at 15 km landward [*Ellis et al.*, 2015]. The modeling results of Ellis et al. [2015] along line 05CM-04 show that excess fluid pressure exists at the updip and downdip ends of a subducted seamount. The over-pressure anomaly at the updip end of the seamount is 5–8 km deep and 6–13

km from the deformation front, in proximity of the splay fault system surfacing landward of the deformation front at the heat flow measurement site. Their model shows the over-pressure location to be a source of fluid that finds escape along the decollement, but splay faults are not included in the model.

Fluid generation from smectite to illite conversion is thermally influenced, occurring at approximately ~60°–150°C, with 75% completion occurring from ~80°–135°C [*Ellis et al.*, 2015]. Figure 13b shows estimated temperatures along the subduction thrust. The location of the 100°C isotherm illustrates the location of active illitization along the subduction thrust. The model results from this study place the 100°C isotherm between 40–50 km for the range of μ' from 0 to 0.03. These results are in general agreement with Ellis et al. [2015] and suggests that illitization is downdip of compaction sourced fluid. These compaction-sourced fluids are in closer proximity to the splay system feeding our heat flow measurement sites and are considered to be an order of magnitude more significant in producing fluids than illitization [*Ellis et al.*, 2015], indicating that the fluids contributing thermally to the heat flow anomalies observed landward of the deformation front are from compaction.

Slow slip events occur in this region of the northern Hikurangi from near the deformation front to depths of ~22 km. These events are hypothesized to be due to overpressures along the subduction thrust. My thermal results suggest that fluids causing overpressures are dominantly from compaction for the shallow portion of this range but that fluids from smectite dehydration may be contributing to overpressures at the deeper region of observed slow slip. Overpressures are not inconsistent with my interpretation of advective fluid flow as long as the source flux is larger than the discharge flux.

Previous studies have inferred that SSEs are associated with fluid overpressuring along the subduction thrust fault [*Bell et al.*, 2010; *Kitajima and Saffer*, 2012; *Kodaira et al.*, 2004] and that such an overpressure setting is present

at the northern Hikurangi margin based on a seismic velocity analysis [Bassett et al., 2014]. Also, faulting in the northern Hikurangi margin has been inferred to be permeable, facilitating the discharge of overpressured fluids [*Ellis et al.*, 2015]. These previous studies are consistent with my interpretation that the heat flow data presented in this study requires the occurrence of advective fluid flow through the margin along permeable splay faults sourced from a deeper, warmed region of overpressuring. These previous studies are also consistent with my finding of a low effective coefficient of friction that requires high pore fluid ratios and overpressures to minimize frictional heating.

8. Conclusions

On the basis of this study I conclude the following:

1. Mean corrected heat flow seaward of the deformation front is ~58 mW m^{-2}. This is slightly higher than the mean GDH1 prediction of 50 mW m^{-2} for lithosphere 120 Myr, but still within the range of uncertainty given the variability in GDH1 parameters for lithosphere thickness (± 15 km) and basal temperature (± 250°C).

2. Advective heat flow appears locally significant. Evidence of fluid recharge is conspicuous on the Tūranganui heat flow transect and the inverse correlation between sediment thickness and heat flow just seaward of the deformation front suggests that the basement/sediment interface is nearly isothermal. However, the correlation between the mean of our observed values and GDH1 indicates that significant quantities of heat are not being advected into the ocean. That is, advective fluid flow is only locally significant.

3. No likely combination of parameters in our conductive 2-D model can duplicate the mean landward heat flow observations of 44 mW m^{-2}, as the 2-D model predicts a depressed heat flow immediately landward of the deformation front. Also I am not able to duplicate the local heat flow anomalies landward of

the deformation front along line 05CM-04 near CDP 4009 and 4300. Parameters not implemented in this model include fluid flow through the forearc toe. Future work in 2-D and conductive and fluid flow modelling may confirm the cause of the elevated heat flow, which I conclude to be advection of compaction generated fluid at shallow depths.

4. Heat flow data from previous authors fits the 2-D model heat flow at 80–180 km landward of the deformation front with best RMS fits for coefficient of friction values of 0.13–0.18. Although the RMS fit of all heat flow data landward of the deformation front is best for coefficient of friction values of 0.18, much of these data are well above the relatively high coefficient of friction of 0.18 and are best explained by warmed fluid discharge in splay faults. The lower heat flow values observed landward of the deformation front are more likely representative of the conductive regime of the forearc, fitting to the model with μ' values of 0.0–0.03. This suggests that lower coefficients of friction exist within 12 km landward of the deformation front, while higher coefficients of friction exist higher coefficient of friction exist farther landward (80–180 km).

5. The fluid driving the elevated heat flow landward of the deformation front requires a source, which is likely from compaction of sediment in the trailing end of a subducting seamount within several km's of the base of the splay fault system. Clay mineral dehydration occurs shallower and nearer to the deformation front than modelled in previous work, with the extent of illitization limited to 10–65 km from the deformation front, depending on coefficient of friction, placing illitization entirely within the zone of SSE occurrence. The model results from this study place the 100°C isotherm at 40–50 km respectively for values of 0.00 and 0.03, which is shallower than the 45 km predicted by Ellis et al. [2015] but still downdip of the location of fluid generated by compaction, and not likely to contribute significantly to fluid discharge at the heat flow measurement site.

9. Bibliography

Ansell, J. H., and S. C. Bannister (1996), Shallow morphology of the subducted Pacific plate along the Hikurangi margin, New Zealand, *Phys Earth Planet In*, *93*(1-2), 3-20.

Ballance, P. F. (1976), Evolution of Upper Cenozoic Magmatic Arc and Plate Boundary in Northern New-Zealand, *Earth Planet Sc Lett*, *28*(3), 356-370.

Barker, D. H. N., R. Sutherland, S. Henrys, and S. Bannister (2009), Geometry of the Hikurangi subduction thrust and upper plate, North Island, New Zealand, *Geochem Geophy Geosy*, *10*.

Barnes, P. M., G. Lamarche, J. Bialas, S. Henrys, I. Pecher, G. L. Netzeband, J. Greinert, J. J. Mountjoy, K. Pedley, and G. Crutchley (2010), Tectonic and geological framework for gas hydrates and cold seeps on the Hikurangi subduction margin, New Zealand, *Mar Geol*, *272*(1-4), 26-48.

Bassett, D., R. Sutherland, and S. Henrys (2014), Slow wavespeeds and fluid overpressure in a region of shallow geodetic locking and slow slip, Hikurangi subduction margin, New Zealand, *Earth Planet Sc Lett*, *389*, 1-13.

Bassett, D., R. Sutherland, S. Henrys, T. Stern, M. Scherwath, A. Benson, S. Toulmin, and M. Henderson (2010), Three-dimensional velocity structure of the northern Hikurangi margin, Raukumara, New Zealand: Implications for the growth of continental crust by subduction erosion and tectonic underplating, *Geochem Geophy Geosy*, *11*.

Bell, R., R. Sutherland, D. H. N. Barker, S. Henrys, S. Bannister, L. Wallace, and J. Beavan (2010), Seismic reflection character of the Hikurangi subduction interface, New Zealand, in the region of repeated Gisborne slow slip events, *Geophys J Int*, *180*(1), 34-48.

Bullard, E. (1939), Heat flow in South Africa, *Proceedings of the Royal Society of London. Series A, Mathematical and Physical Sciences*, 474-502.

Byerlee, J. (1978), Friction of Rocks, *Pure Appl Geophys*, *116*(4-5), 615-626.

Caristan, Y. (1982), The Transition from High-Temperature Creep to Fracture in Maryland Diabase, *J Geophys Res*, *87*(Nb8), 6781-6790.

Carslaw, H. S., and J. C. Jaeger (1959), *Conduction of heat in solids*, Clarendon Press, Oxford.

Carter, L., C. S. Nelson, H. L. Neil, and P. C. Froggatt (1995), Correlation, Dispersal, and Presentation of the Kawakawa Tephra and Other Late Quaternary Tephra Layers in the Southwest Pacific-Ocean, *New Zeal J Geol Geop*, *38*(1), 29-46.

Collot, J. Y., K. Lewis, G. Lamarche, and S. Lallemand (2001), The giant Ruatoria debris avalanche on the northern Hikurangi margin, New Zealand: Result of oblique seamount subduction, *J Geophys Res-Sol Ea*, *106*(B9), 19271-19297.

Collot, J. Y., et al. (1996), From oblique subduction to intra-continental transpression: Structures of the southern Kermadec-Hikurangi margin from multibeam bathymetry, side-scan sonar and seismic reflection, *Mar Geophys Res*, *18*(2-4), 357-381.

Currie, C. A., and R. D. Hyndman (2006), The thermal structure of subduction zone back arcs, *J Geophys Res-Sol Ea*, *111*(B8).

Currie, C. A., R. D. Hyndman, K. Wang, and V. Kostoglodov (2002), Thermal models of the Mexico subduction zone: Implications for the megathrust seismogenic zone, *J Geophys Res-Sol Ea*, *107*(B12).

Davis, E. E., K. L. Wang, J. H. He, D. S. Chapman, H. Villinger, and A. Rosenberger (1997), An unequivocal case for high Nusselt number hydrothermal convection in sediment-buried igneous oceanic crust, *Earth Planet Sc Lett*, *146*(1-2), 137-150.

Davy, B., and R. Wood (1994), Gravity and Magnetic Modeling of the Hikurangi Plateau, *Mar Geol*, *118*(1-2), 139-151.

Davy, B., K. Hoernle, and R. Werner (2008), Hikurangi Plateau: Crustal structure, rifted formation, and Gondwana subduction history, *Geochem Geophy Geosy*, *9*.

DeMets, C., R. G. Gordon, and D. F. Argus (2010), Geologically current plate motions, *Geophys J Int*, *181*(1), 1-80.

Douglas, A., J. Beavan, L. Wallace, and J. Townend (2005), Slow slip on the northern Hikurangi subduction interface, New Zealand, *Geophys Res Lett*, *32*(16).

Dragert, H., K. L. Wang, and T. S. James (2001), A silent slip event on the deeper Cascadia subduction interface, *Science*, *292*(5521), 1525-1528.

Ellis, S., A. Fagereng, D. Barker, S. Henrys, D. Saffer, L. Wallace, C. Williams, and R. Harris (2015), Fluid budgets along the northern Hikurangi subduction margin, New Zealand: the effect of a subducting seamount on fluid pressure, *Geophys J Int*, *202*(1), 277-297.

Fagereng, A. (2011), Wedge geometry, mechanical strength, and interseismic coupling of the Hikurangi subduction thrust, New Zealand, *Tectonophysics*, *507*(1-4), 26-30.

Fagereng, A., and S. Ellis (2009), On factors controlling the depth of interseismic coupling on the Hikurangi subduction interface, New Zealand, *Earth Planet Sc Lett*, *278*(1-2), 120-130.

Field, B. D., and C. Uruski (1997), *Cretaceous-Cenozoic geology and petroleum systems of the East Coast region, New Zealand*, Institute of Geological & Nuclear Sciences.

Fisher, A. T., and R. P. Von Herzen (2005), Models of hydrothermal circulation within 106 Ma seafloor: Constraints on the vigor of fluid circulation and crustal properties, below the Madeira Abyssal Plain, *Geochem Geophy Geosy*, *6*.

Fulton, P. M., et al. (2013), Low Coseismic Friction on the Tohoku-Oki Fault Determined from Temperature Measurements, *Science*, *342*(6163), 1214-1217.

Gao, X., and K. L. Wang (2014), Strength of stick-slip and creeping subduction megathrusts from heat flow observations, *Science*, *345*(6200), 1038-1041.

Harris, R. N., A. T. Fisher, and D. S. Chapman (2004), Fluid flow through seamounts and implications for global mass fluxes, *Geology*, *32*(8), 725-728.

Harris, R. N., G. Spinelli, C. R. Ranero, I. Grevemeyer, H. Villinger, and U. Barckhausen (2010), Thermal regime of the Costa Rican convergent margin: 2. Thermal models of the shallow Middle America subduction zone offshore Costa Rica, *Geochem Geophy Geosy*, *11*.

Harris, R. N., et al. (2015), Cruise Report, STINGS Expedition R/V Roger Revelle, RR1508, 16 May–18 June, "The Thermal Regime of the Hikurangi Subduction Zone and Shallow Slow Slip Events, New Zealand"*Rep.*

Hartmann, A., and H. Villinger (2002), Inversion of marine heat flow measurements by expansion of the temperature decay function, *Geophys J Int*, *148*(3), 628-636.

Hass, B., and R. N. Harris (2016), Heat flow along the Costa Rica Seismogenesis Project drilling transect: Implications for hydrothermal and seismic processes, *Geochem Geophy Geosy*, *17*(6), 2110-2127.

Henrys, S., S. Ellis, and C. Uruski (2003), Conductive heat flow variations from bottom-simulating reflectors on the Hikurangi margin, New Zealand, *Geophys Res Lett*, *30*(2).

Henrys, S., P. Barnes, D. Saffer, J. Mountjoy, L. Wallace, M. Underwood, and M. Torres (2013), Safety review report for IODP proposal 781A-Full: Unlocking the secrets of slow slip by drilling at the northern Hikurangi subduction margin, New Zealand*Rep.*, GNS.

Hirose, H., K. Hirahara, F. Kimata, N. Fujii, and S. Miyazaki (1999), A slow thrust slip event following the two 1996 Hyuganada earthquakes beneath the Bungo Channel, southwest Japan, *Geophys Res Lett*, *26*(21), 3237-3240.

Hoernle, K., F. Hauff, P. van den Bogaard, R. Werner, N. Mortimer, J. Geldmacher, D. Garbe-Schonberg, and B. Davy (2010), Age and geochemistry of volcanic rocks from the Hikurangi and Manihiki oceanic Plateaus, *Geochim Cosmochim Ac*, *74*(24), 7196-7219.

Hutnak, M., and A. T. Fisher (2007), Influence of sedimentation, local and regional hydrothermal circulation, and thermal rebound on measurements of seafloor heat flux, *J Geophys Res-Sol Ea*, *112*(B12).

Hyndman, R. D., and K. Wang (1993), Thermal Constraints on the Zone of Major Thrust Earthquake Failure - the Cascadia Subduction Zone, *J Geophys Res-Sol Ea*, *98*(B2), 2039-2060.

Hyndman, R. D., E. E. Davis, and J. A. Wright (1979), Measurement of Marine Geothermal Heat-Flow by a Multi-Penetration Probe with Digital Acoustic Telemetry and Insitu Thermal-Conductivity, *Mar Geophys Res*, *4*(2), 181-205.

Kitajima, H., and D. M. Saffer (2012), Elevated pore pressure and anomalously low stress in regions of low frequency earthquakes along the Nankai Trough subduction megathrust, *Geophys Res Lett*, *39*.

Kodaira, S., T. Iidaka, A. Kato, J. O. Park, T. Iwasaki, and Y. Kaneda (2004), High pore fluid pressure may cause silent slip in the Nankai Trough, *Science*, *304*(5675), 1295-1298.

Kroenke, L., P. Wessel, and A. Sterling (2004), Motion of the Ontong Java Plateau in the hot-spot frame of reference: 122 Ma-present, *Geological Society, London, Special Publications*, *229*(1), 9-20.

Lachenbruch, A. H., and J. H. Sass (1980), Heat-Flow and Energetics of the San-Andreas Fault Zone, *J Geophys Res*, *85*(Nb11), 6185-6222.

Lewis, K. B. (1994), The 1500-Km-Long Hikurangi Channel - Trench-Axis Channel That Escapes Its Trench, Crosses a Plateau, and Feeds a Fan Drift, *Geo-Mar Lett*, *14*(1), 19-28.

Lewis, K. B., and B. P. Kohn (1973), Ashes, Turbidites, and Rates of Sedimentation on Continental Slope Off Hawkes-Bay, *New Zeal J Geol Geop*, *16*(3), 439-454.

Lewis, K. B., and H. M. Pantin (2002), Channel-axis, overbank and drift sediment waves in the southern Hikurangi Trough, New Zealand, *Mar Geol*, *192*(1-3), 123-151.

Lewis, K. B., J. Y. Collot, and S. E. Lallemand (1998), The dammed Hikurangi Trough: a channel-fed trench blocked by subducting seamounts and their wake avalanches (New Zealand-France GeodyNZ Project), *Basin Res*, *10*(4), 441-468.

Liu, Y. J., and J. R. Rice (2007), Spontaneous and triggered aseismic deformation transients in a subduction fault model, *J Geophys Res-Sol Ea*, *112*(B9).

McCaffrey, R., L. M. Wallace, and J. Beavan (2008), Slow slip and frictional transition at low temperature at the Hikurangi subduction zone, *Nat Geosci*, *1*(5), 316-320.

Moore, J. C., and D. Saffer (2001), Updip limit of the seismogenic zone beneath the accretionary prism of southwest Japan: An effect of diagenetic to low-grade metamorphic processes and increasing effective stress, *Geology*, *29*(2), 183-186.

Mortimer, N., K. Hoernle, F. Hauff, J. M. Palin, W. J. Dunlap, R. Werner, and K. Faure (2006), New constraints on the age and evolution of the Wishbone Ridge, southwest Pacific Cretaceous microplates, and Zealandia-West Antarctica breakup, *Geology*, *34*(3), 185-188.

Obara, K., H. Hirose, F. Yamamizu, and K. Kasahara (2004), Episodic slow slip events accompanied by non-volcanic tremors in southwest Japan subduction zone, *Geophys Res Lett*, *31*(23).

Oleskevich, D. A., R. D. Hyndman, and K. Wang (1999), The updip and downdip limits to great subduction earthquakes: Thermal and structural models of Cascadia, south Alaska, SW Japan, and Chile, *J Geophys Res-Sol Ea*, *104*(B7), 14965-14991.

Peacock, S. M., and K. Wang (1999), Seismic consequences of warm versus cool subduction metamorphism: Examples from southwest and northeast Japan, *Science*, *286*(5441), 937-939.

Pedley, K. L., P. M. Barnes, J. R. Pettinga, and K. B. Lewis (2010), Seafloor structural geomorphic evolution of the accretionary frontal wedge in response to seamount subduction, Poverty Indentation, New Zealand, *Mar Geol*, *270*(1-4), 119-138.

Plaza-Faverola, A., D. Klaeschen, P. Barnes, I. Pecher, S. Henrys, and J. Mountjoy (2012), Evolution of fluid expulsion and concentrated hydrate zones across the southern Hikurangi subduction margin, New Zealand: An analysis from depth migrated seismic data, *Geochem Geophy Geosy*, *13*.

Pouderoux, H., J. N. Proust, G. Lamarche, A. Orpin, and H. Neil (2012), Postglacial (after 18 ka) deep-sea sedimentation along the Hikurangi subduction margin (New Zealand): Characterisation, timing and origin of turbidites, *Mar Geol*, *295*, 51-76.

Powell, W., D. Chapman, N. Balling, and A. Beck (1988), Continental heat-flow density, in *Handbook of terrestrial heat-flow density determination*, edited, pp. 167-222, Springer.

Reyners, M., D. Eberhart-Phillips, and S. Bannister (2011), Tracking repeated subduction of the Hikurangi Plateau beneath New Zealand, *Earth Planet Sc Lett*, *311*(1-2), 165-171.

Ryan, W. B. F., et al. (2009), Global Multi-Resolution Topography synthesis, *Geochem Geophy Geosy*, *10*.

Schwartz, S. Y., and J. M. Rokosky (2007), Slow slip events and seismic tremor at circum-pacific subduction zones, *Rev Geophys*, *45*(3).

Shipboard Scientific Party (1999a), Site 1123: North Chatham Drift—a 20-Ma record of the Pacific Deep Western Boundary Current. In Carter, R.M., McCave, I.N., Richter, C., Carter, L., et al., Proc. ODP, Init. Repts., 181: College Station, TX (Ocean Drilling Program), 1–184. *Rep.*

Shipboard Scientific Party (1999b), Site 1124: Rekohu Drift—from the K/T boundary to the Deep Western Boundary Current. In Carter, R.M., McCave, I.N., Richter, C., Carter, L., et al., Proc. ODP, Init. Repts., 181: College Station, TX (Ocean Drilling Program), 1–137. .

Stein, C. A., and S. Stein (1992), A Model for the Global Variation in Oceanic Depth and Heat-Flow with Lithospheric Age, *Nature*, *359*(6391), 123-129.

Stein, C. A., and S. Stein (1994), Constraints on Hydrothermal Heat-Flux through the Oceanic Lithosphere from Global Heat-Flow, *J Geophys Res-Sol Ea*, *99*(B2), 3081-3095.

Taylor, B. (2006), The single largest oceanic plateau: Ontong Java-Manihiki-Hikurangi, *Earth Planet Sc Lett*, *241*(3-4), 372-380.

Tejada, M. L. G., J. J. Mahoney, C. R. Neal, R. A. Duncan, and M. G. Petterson (2002), Basement geochemistry and geochronology of central Malaita, Solomon islands, with implications for the origin and evolution of the Ontong Java Plateau, *J Petrol*, *43*(3), 449-484.

Townend, J. (1997), Estimates of conductive heat flow through bottom-simulating reflectors on the Hikurangi and southwest Fiordland continental margins, New Zealand, *Mar Geol*, *141*(1-4), 209-220.

Villinger, H., and E. E. Davis (1987), A New Reduction Algorithm for Marine Heat-Flow Measurements, *J Geophys Res-Solid*, *92*(B12), 12846-12856.

Walcott, R. I. (1987), Geodetic Strain and the Deformational History of the North-Island of New-Zealand during the Late Cainozoic, *Philos T R Soc A*, *321*(1557), 163-181.

Wallace, L. M., and J. Beavan (2006), A large slow slip event on the central Hikurangi subduction interface beneath the Manawatu region, North Island, New Zealand, *Geophys Res Lett*, *33*(11).

Wallace, L. M., and J. Beavan (2010), Diverse slow slip behavior at the Hikurangi subduction margin, New Zealand, *J Geophys Res-Sol Ea*, *115*.

Wallace, L. M., J. Beavan, R. McCaffrey, and D. Darby (2004), Subduction zone coupling and tectonic block rotations in the North Island, New Zealand, *J Geophys Res-Sol Ea*, *109*(B12).

Wallace, L. M., J. Beavan, S. Bannister, and C. Williams (2012), Simultaneous long-term and short-term slow slip events at the Hikurangi subduction margin, New Zealand:

Implications for processes that control slow slip event occurrence, duration, and migration, *J Geophys Res-Sol Ea*, *117*.

Wallace, L. M., S. C. Webb, Y. Ito, K. Mochizuki, R. Hino, S. Henrys, S. Y. Schwartz, and A. F. Sheehan (2016), Slow slip near the trench at the Hikurangi subduction zone, New Zealand, *Science*, *352*(6286), 701-704.

Wang, K. L., R. D. Hyndman, and M. Yamano (1995), Thermal Regime of the Southwest Japan Subduction Zone - Effects of Age History of the Subducting Plate, *Tectonophysics*, *248*(1-2), 53-69.

Williams, C. A., D. Eberhart-Phillips, S. Bannister, D. H. N. Barker, S. Henrys, M. Reyners, and R. Sutherland (2013), Revised Interface Geometry for the Hikurangi Subduction Zone, New Zealand, *Seismol Res Lett*, *84*(6), 1066-1073.

Wood, R., and B. Davy (1994), The Hikurangi Plateau, *Mar Geol*, *118*(1-2), 153-173.

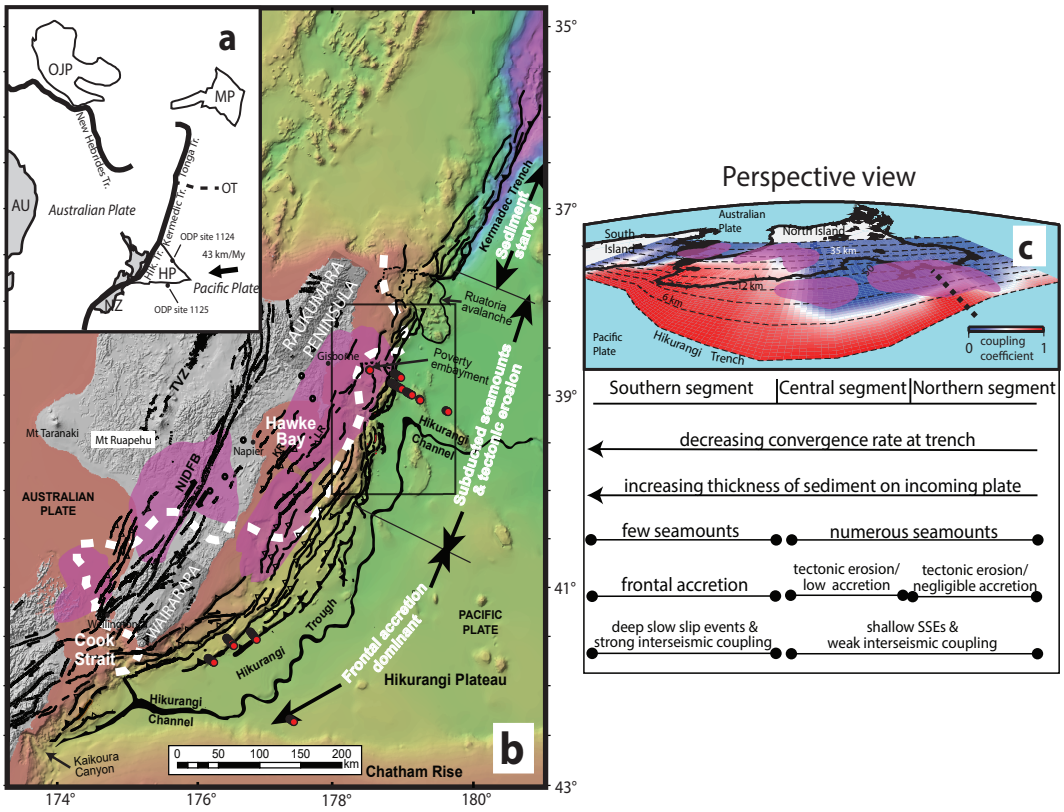

Figure 1. Tectonic setting of the North Island, New Zealand. a) New Zealand in relation to southwest Pacific tectonics and locations of Ontong Java (OP), Manihiki (MP), and Hikurangi (HP) plateaus and Osbourne Trough (OT) (modified from Taylor 2006). Black arrow shows convergence rate and azimuth. b) Detailed bathymetry, topography, and active faulting of the onshore and offshore margin (modified from Wallace et al. 2009). Bold white dashed line shows position of 20 mm yr^{-1} slip deficit (Wallace et al 2004). Magenta areas show regions of observed slow slip events. Box outlines location of heat flow measurements presented in this study. Red circles show approximate heat flow measurement locations during cruise RR1508. TVZ indicates Taupo Volcanic Zone. c) Perspective view looking northwest across the Hikurangi margin and North Island New Zealand illustrating the portions of the subduction interface that undergo stick-slip and aseismic slip in terms of coupling coefficient (modified from Wallace and Beavan 2010). Coupling coefficient values of one indicate locked areas, while values of zero indicate steady aseismic slip. Purple patches show areas of slip in slow slip events since 2002. Along strike variations in convergent margin properties are summarized below the map.

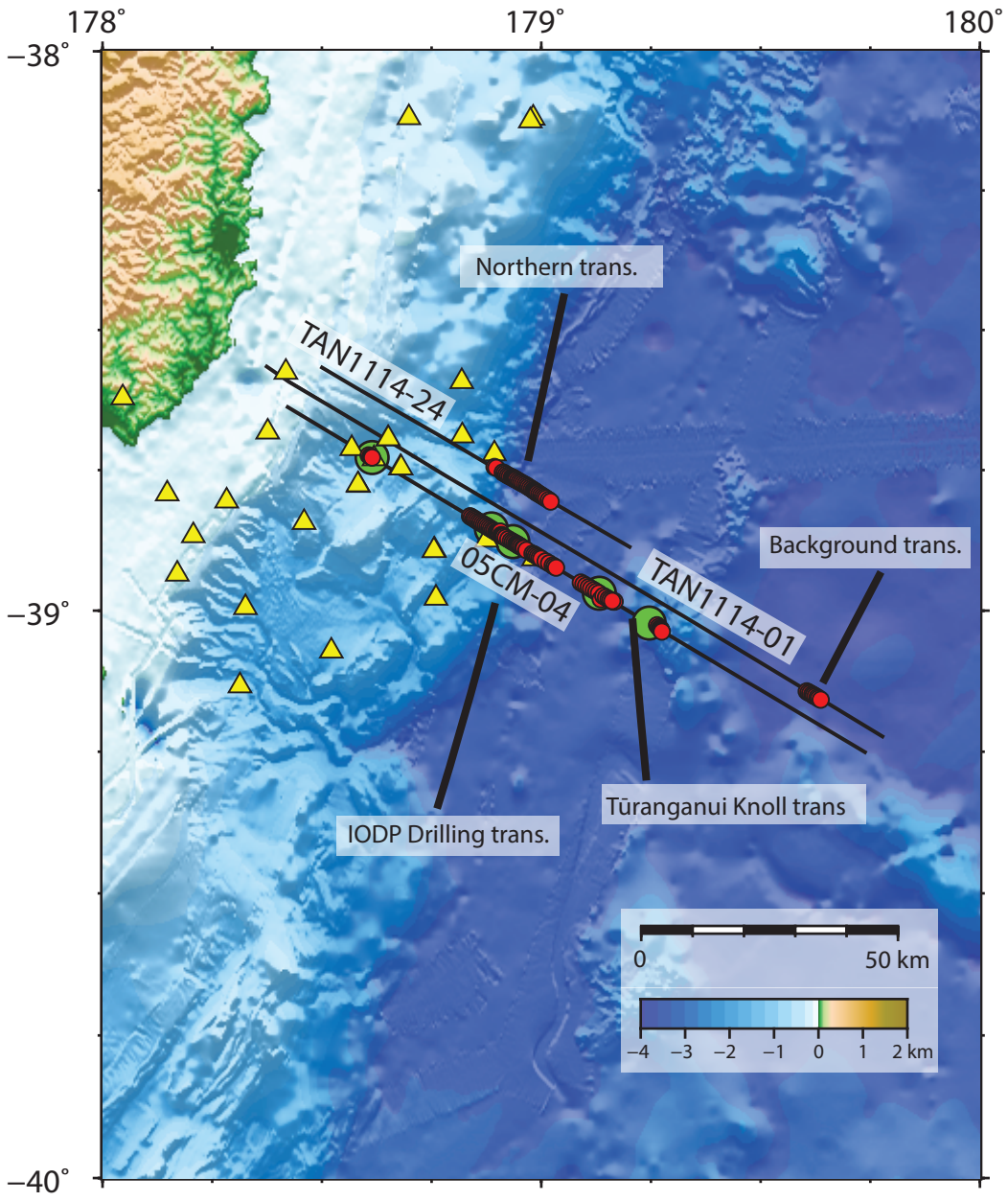

Figure 2. Locations of northern Hikurangi heat flow measurements (red circles) collocated with labeled seismic lines (black lines). This figure is an expanded view of the boxed portion of Figure 1b. Bottom water temperature intsruments are emplaced onboard OBS and APGs (yellow triangles) distributed about the Poverty Indentation to collect data for ~1 year preceding the heat flow measurements. Proposed IODP drilling sites (green circles) are along line 05CM-04. Heat flow transects discussed in text are labelled. Colorbar represents topography in km relative to sea level.

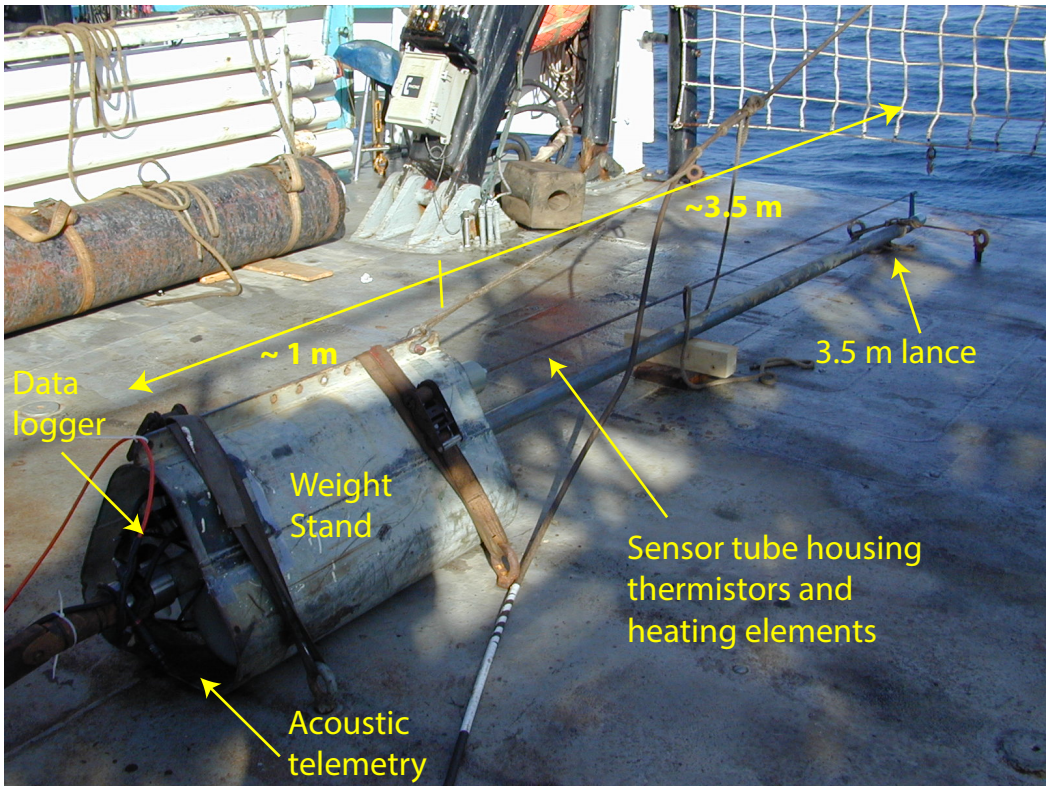

Figure 3. Multipenetration heat flow probe used to collect heat flow measurements.

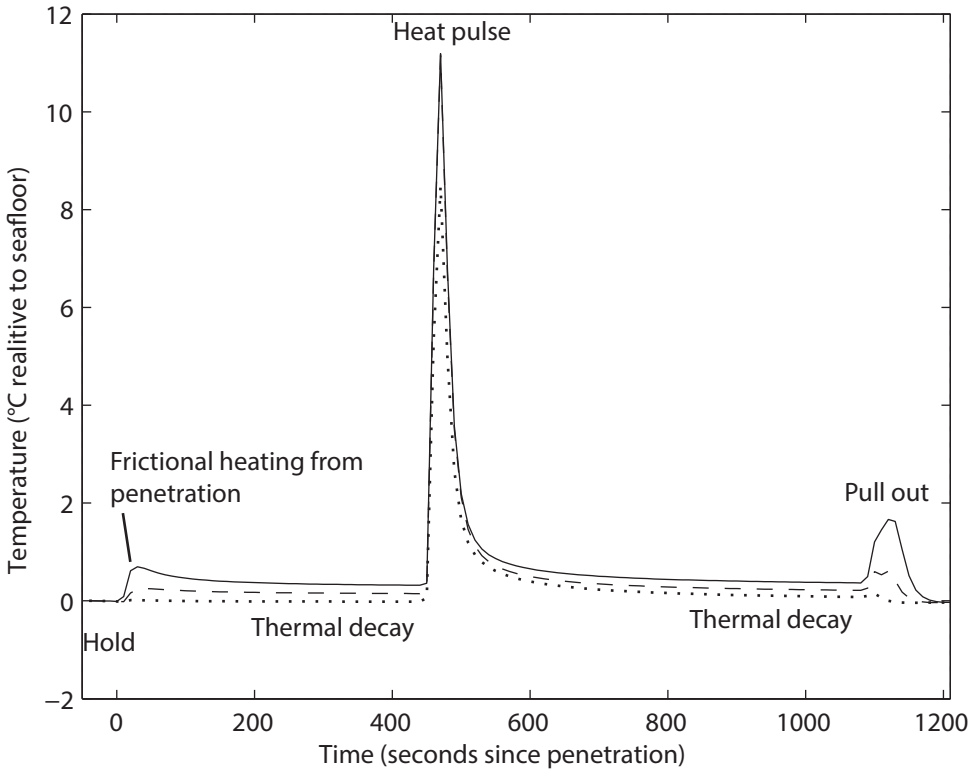

Figure 4. Time series showing the temperature response during single heat flow measurement. Of the 11 sets of temperature data recorded, only those corresponding to the deepest (solid line), middle (dashed line), and shallowest (dotted line) temperature sensors are shown for clarity. The time series begins with the probe held in bottom water until lowered to penetrate the seafloor, causing frictional heating that thermally decays towards the equilibrium temperatures. After seven minutes an active heat pulse is fired and the thermal decay is used for the derivation of sediment thermal conductivity. The measurement ends approximately seven minutes after the heat pulse when the probe is pulled out of the sediment indicated by another frictional heating signal.

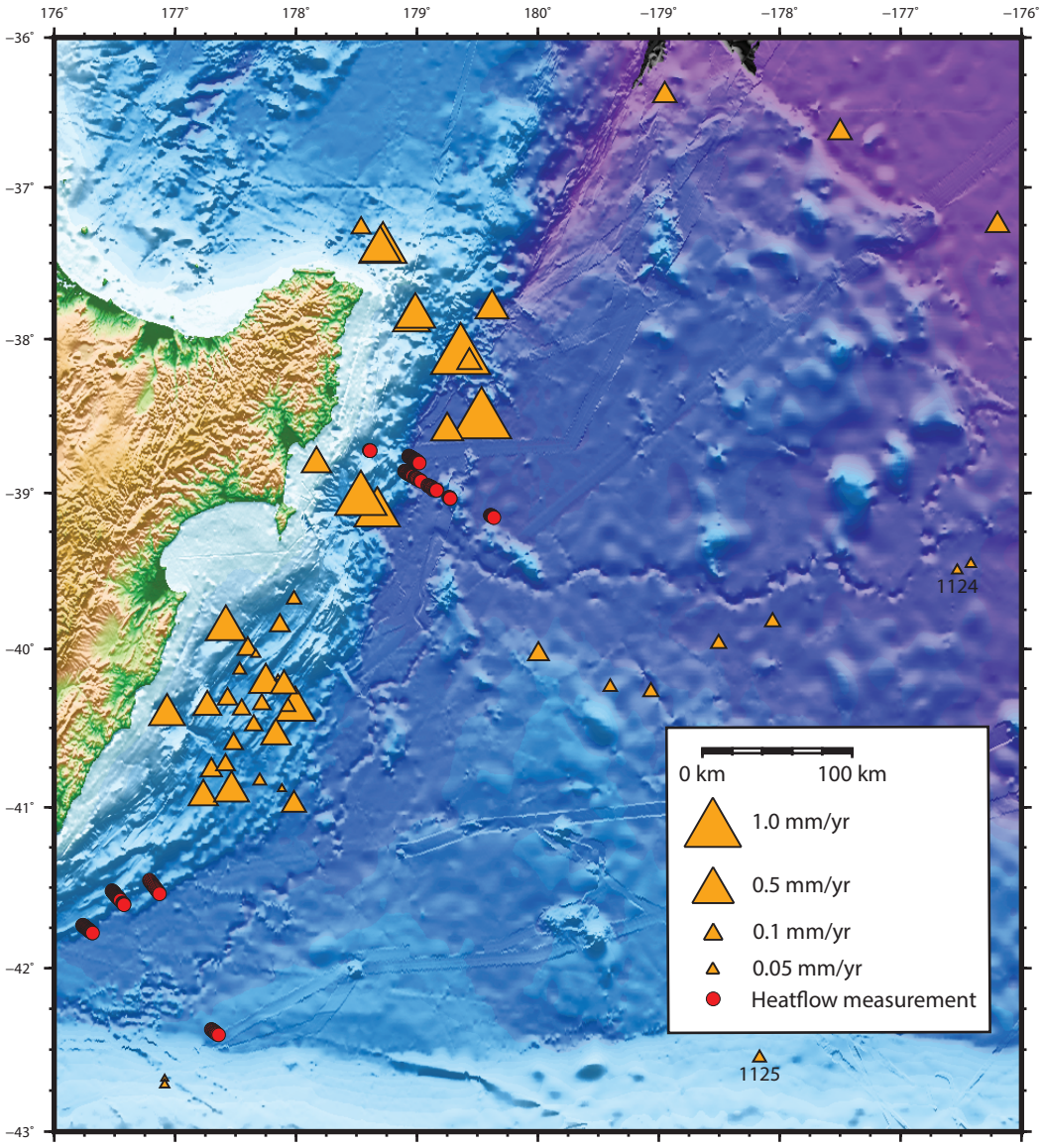

Figure 5. Sediment accumulation rates based on core samples in the Hikurangi trough and plateau. Orange triangles are core locations. Red circles are heat flow measurement locations. Triangle area is proportional to sediment accumulation rate determined. It is apparent that accumulation rates are greater and more consistent the northern Hikurangi than elsewhere, reducing rapidly with increasing distance from the margin. Data from IODP sites 1124 ans 1125 is indicated by site number. Data is from Lewis [1973], Carter et al. [1995], Collot et al. [2001], Pouderoux et al. [2012], Shipboard Scientific Party [1999a, b].

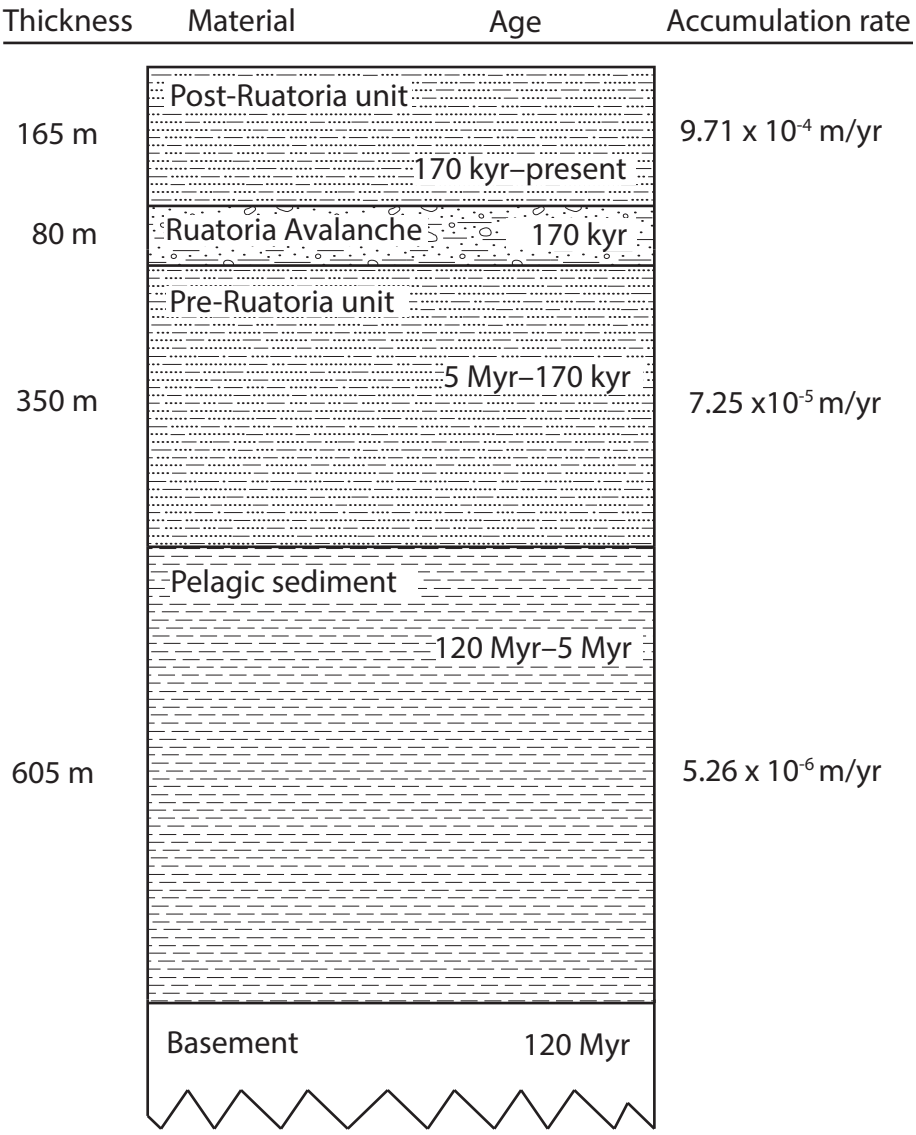

Figure 6. Sedimentation model applied to heat flow measurements seaward of the deformation front. "Basement" is the Hikurangi Plateau large igneous province. "Pelagic sediment" is Mesozoic–Miocene in age. "Pre-Ruatoria unit" is Pliocene–Pleistocene turbidites deposited before the Ruatoia Avalanche. "Post-Ruatoria unit" is Pleistocene–Holocene turbidites deposited after the Ruatoria Avalanche. The sudden emplacement of the Ruatoria Avalanche is modeled as an instantaneous event. Thicknesses of each unit is shown to the left. Emplacement ages are within the diagram. Sediment accumulation rates are shown to the right.

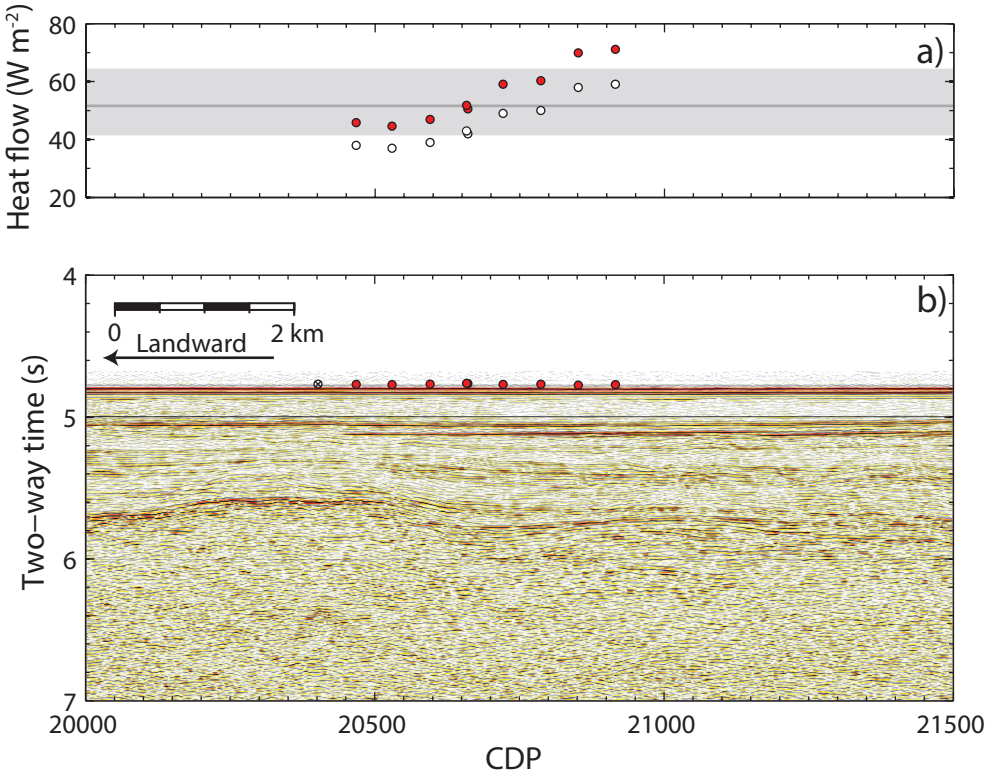

Figure 7. Northern Hikurangi background heat flow site. (a) Heat flow data values. Open circles are raw heat flow data. Red circles also include correction for sedimentation. No bathymetry correction has been applied due to the flat bathymetry. Background heat flow value for oceanic lithosphere this age (120 Myr) is shown as grey dash, based on GDH1 data. b) Location of heat flow measurements. Red circles are successful penetrations. Open circles with crosses did not provide data. Heat flow is in the range of ~59 to 67 mW m^{-2}, with a mean of 63 mW m^{-2}.

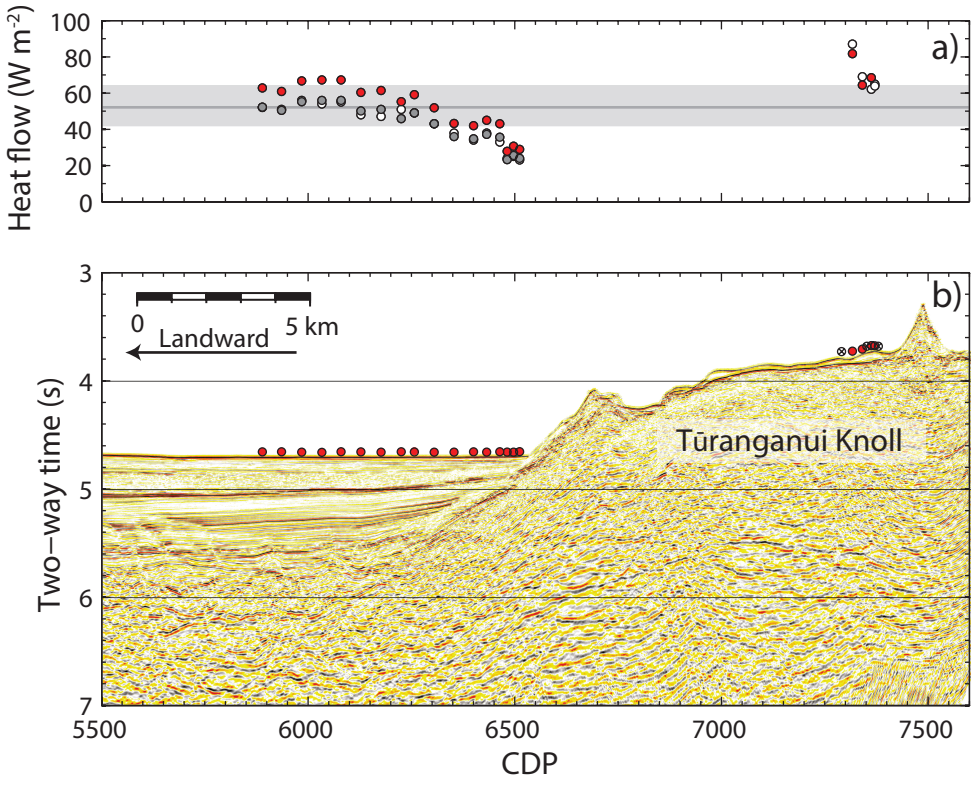

Figure 8. Heat flow data on the Tūranganui Knoll. (a) Heat flow values. Open circles are observed heat flow. Grey circles include the bathymetry correction and red circles also show the sedimentation correction. Grey bar shows predicted heat flow and its uncertainty based on conductive cooling model GDH1 [Stein and Stein, 1992] for 120 Myr age crust. (b) Seismic reflection line 05CM-04. Red circles show successful heat flow measurements and open circles with crosses show unsuccessful measurements.

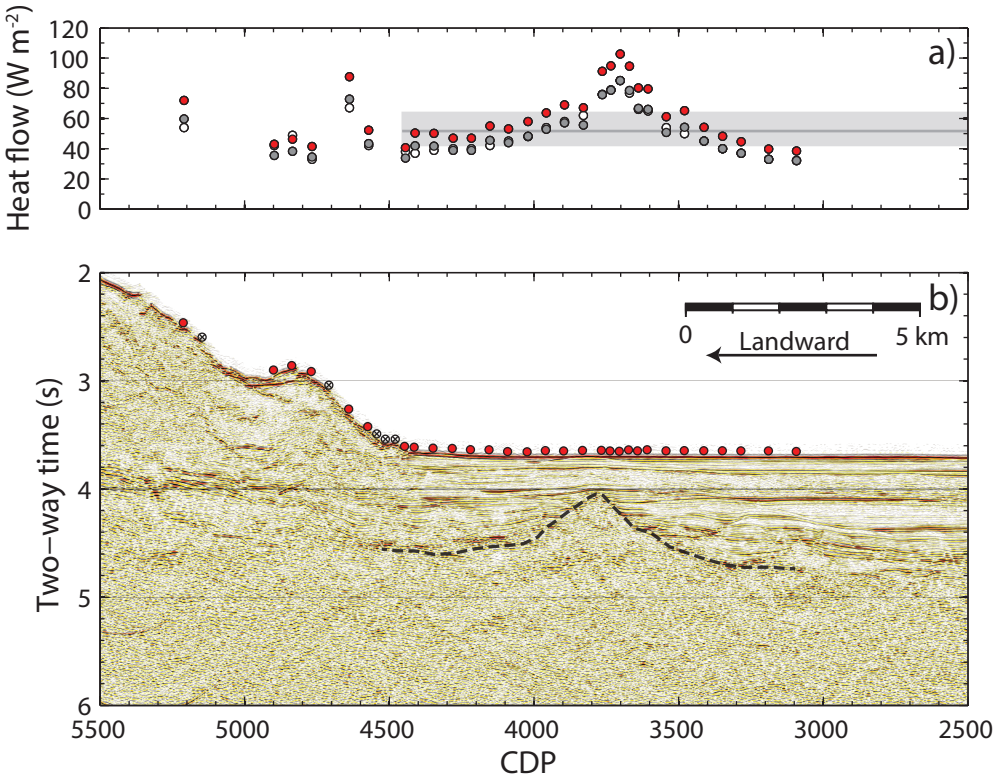

Figure 9. Heat flow data along seismic line TAN1114-24. (a) Heat flow values. Open circles are observed heat flow. Grey circles include the bathymetry correction and red circles also show the sedimentation correction. Grey bar shows predicted heat flow and its uncertainty based on conductive cooling model GDH1 [Stein and Stein, 1992] for 120 Myr age crust. (b) Seismic reflection line TAN1114-24. Red circles show successful heat flow measurements and open circles with crosses show unsuccessful measurements. Dashed black line shows sediment-basement interface.

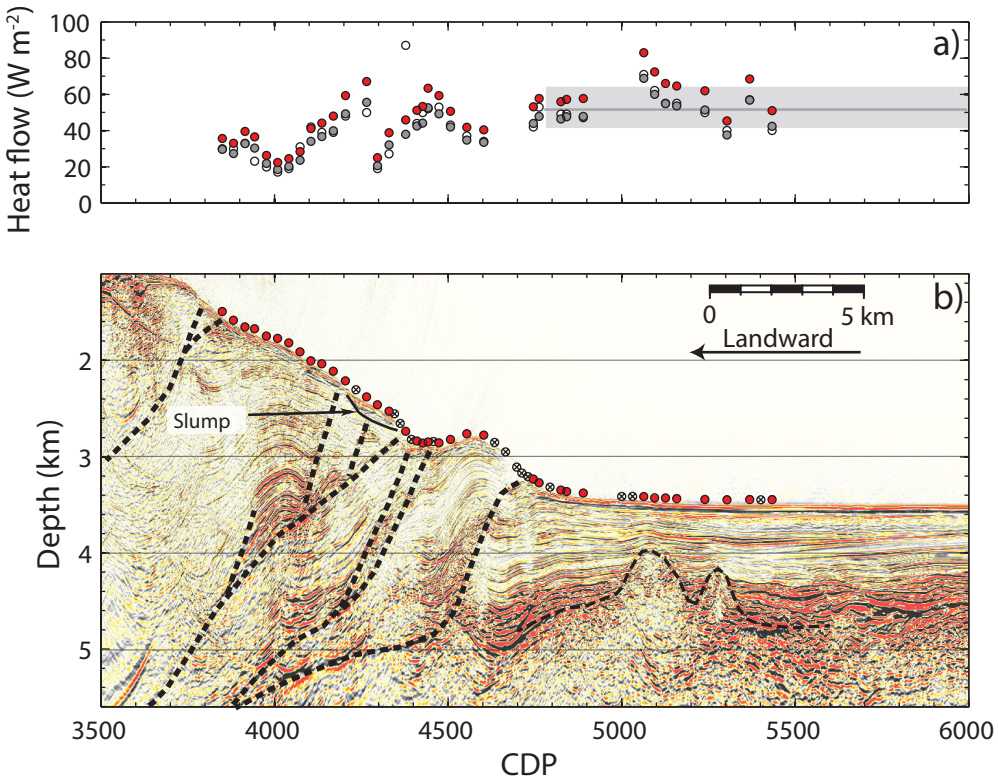

Figure 10. Heat flow data along seismic line 05CM-04. (a) Heat flow values. Open circles are observed heat flow. Grey circles include the bathymetry correction and red circles also show the sedimentation correction. Grey bar shows predicted heat flow and its uncertainty based on conductive cooling model GDH1 [Stein and Stein, 1992] for 120 Myr age crust. (b) Seismic reflection line 05CM-04. Red circles show successful heat flow measurements and open circles with crosses show unsuccessful measurements. Thin dashed black line shows sediment-basement interface. Heavy dashed black lines indicate faults interpreted from Henrys et al. [2013].

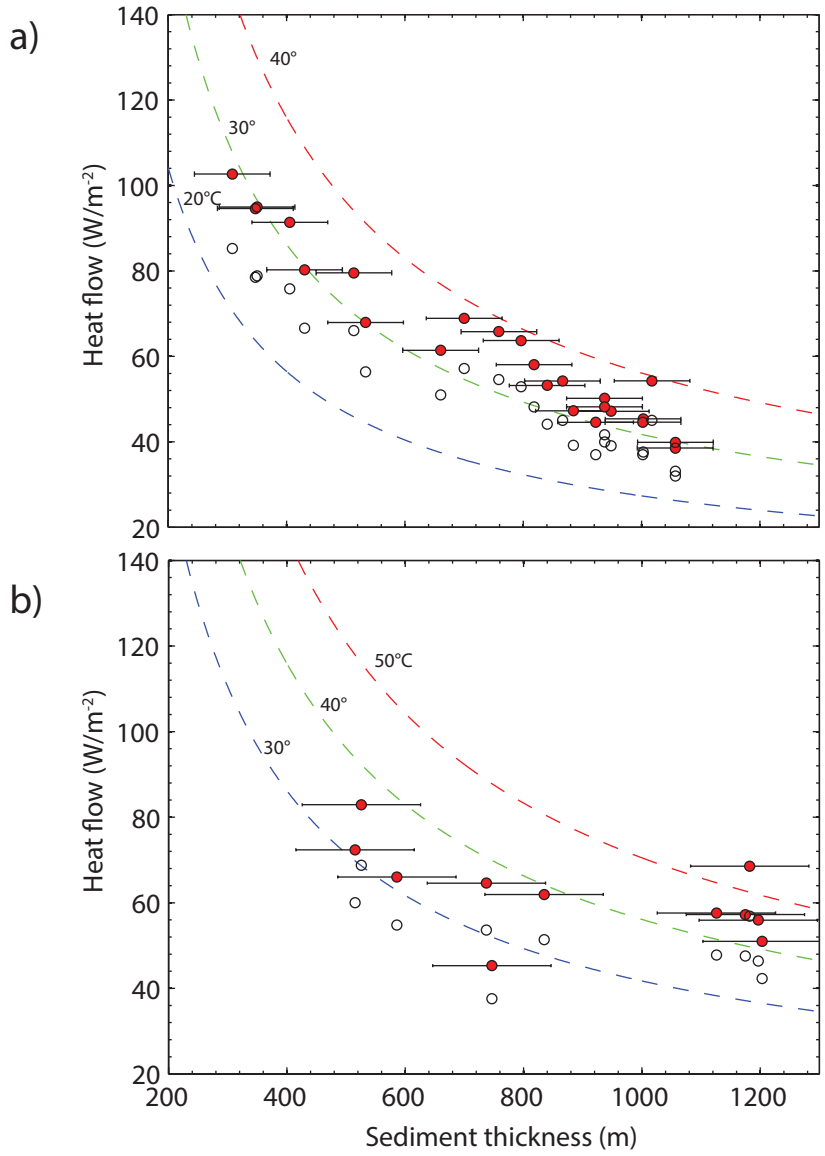

Figure 11. Inverse relationship between heat flow and sediment thickness. Open circles show observed data and red circles show data corrected for both bathymetry and sedimentation. Lines are computed assuming isothermal sediment-basement temperatures. Effects of thermal refraction are not included but are generally small. a) Values along seismic line TAN1114-24 between CDP 3000 to 4500. b) Values along seismic line 05CM-04 between CDP 4800 to 5500.

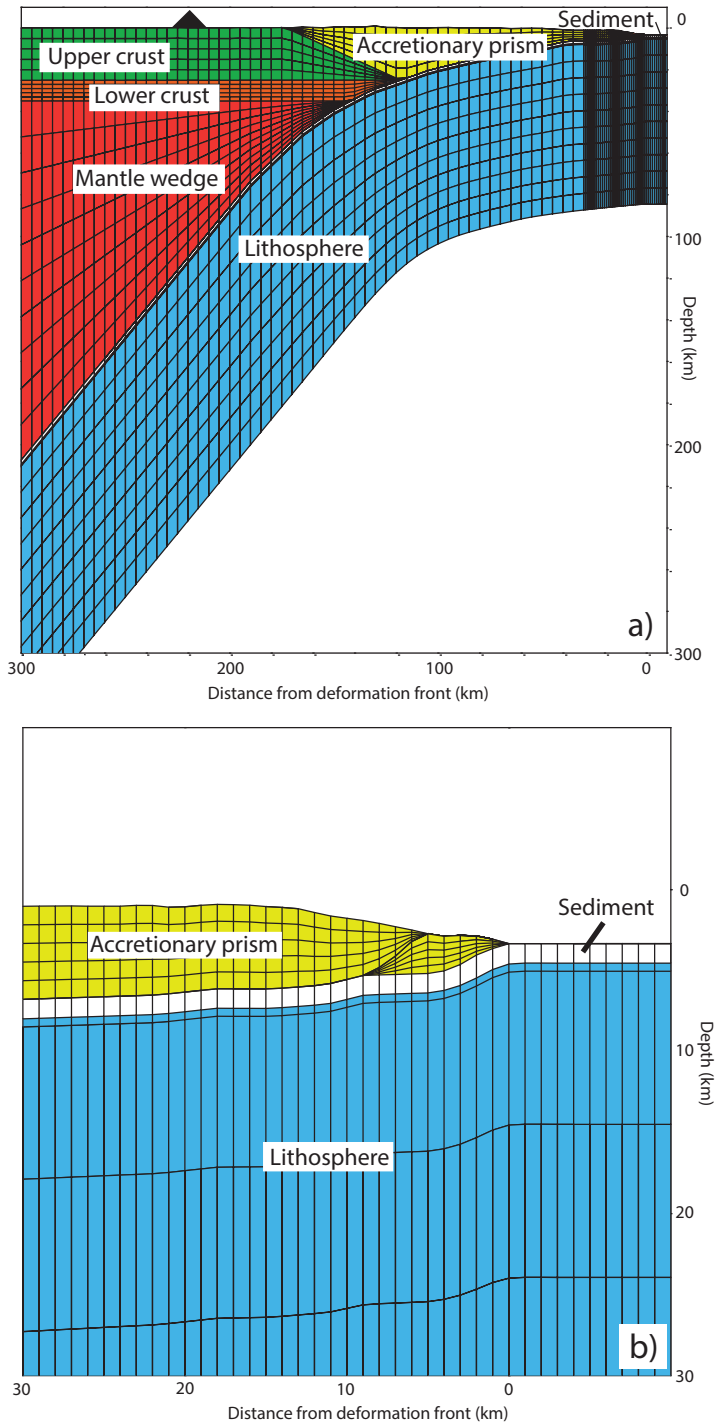

Figure 12. Geometry used for 2-D thermal subduction model. a) Thermophysical units are divided into: accretionary prism (yellow), sediment (white), upper crust (green), lower crust (orange), mantle wedge (red), and oceanic lithosphere (blue). Black triangle indicates location of Taupo Volcanic Zone (TVZ). b) Expanded view of model showing deformation front and splay fault geometry used for sensitivity testing. From 10 km seaward of deformation front to 30 km landward of deformation front a horizontal grid spacing of 1 km is used. Elsewhere, a vertical grid spacing of 5 km is used.

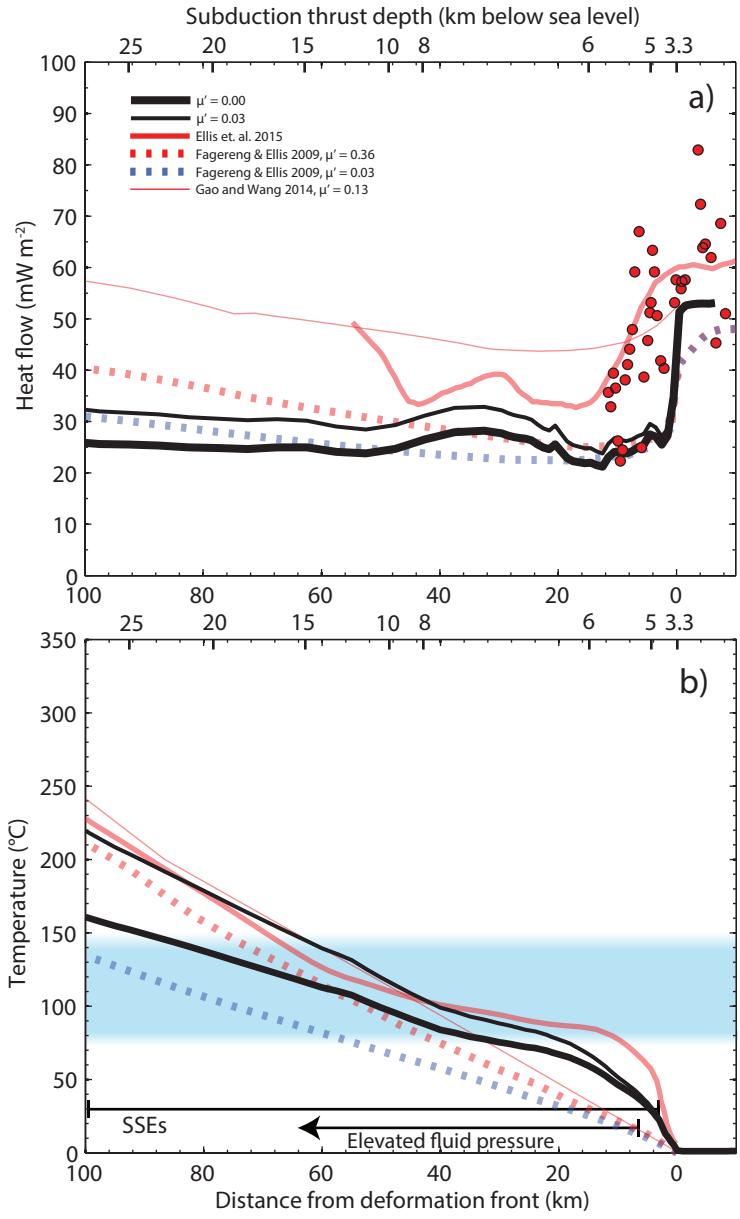

Figure 13. Heat flow and temperature of preferred subduction thrust thermal model. a) Heat flow across the Hikurangi margin along seismic line 05CM-04 (red circles), with model results from this study and by previous authors. b) Temperature along the subduction thrust. Blue zone shows inferred smectite dehydration (75°C) begins at ~10 km and is exhausted (150°C) by ~40 km from deformation front. The location of SSEs (Wallace et al., 2015) is indicated, ending at approximately 100 km from deformation front. The locations of elevated pore fluid pressure are shown (Ellis et al., 2015).

Table 1. Thermal parameters used with SlugSed for sedimentation correction.

Property	Value
Thermal conductivity of lithosphere (W m^{-1} K^{-1})	3.183
Volumetric heat capacity of lithosphere (MJ m^{-3} K^{-1})	3.900
Thermal conductivity of sediment grains (W m^{-1} K^{-1})	2.74
Volumetric heat capacity of sediment grains (MJ m^{-3} K^{-1})	2.65
Thermal conductivity of water (W m^{-1} K^{-1})	0.6
Temperature at surface of plate (°C)	1
Temperature at base of plate (°C)	1450
Lithosphere age (Myr)	120
Lithosphere thickness (km)	80
Athy's Law empirical compaction constant (m^{-1})	8.333×10^{-4}
Athy's Law seafloor porosity	0.7

Table 2. Results of sedimentation analysis.

Stage	Time (Myr)	Thickness (m)	Accum. rate (m yr^{-1})	Correction (%)
Preferred sedimentation correction				
Post-Ruatoria unit	0.17 - present	165	9.71×10^{-4}	9.9
Ruatoria Avalanche	0.17	80	10	2.6
Pre-Ruatoria unit	5 - 0.17	350	7.25×10^{-5}	5.6
Pelagic	120 - 5	605	5.26×10^{-6}	2.4
Total:	120	1200		20.5
High sedimentation correction				
Post-Ruatoria unit	0.17 - present	220	1.29×10^{-3}	12.1
Ruatoria Avalanche	0.17	160	16.0	4.4
Pre-Ruatoria unit	5 - 0.17	400	8.28×10^{-5}	6.7
Pelagic	120 - 5	605	5.26×10^{-6}	2.4
Total:	120	1385		25.5
Low sedimentation correction				
Post-Ruatoria unit	0.17 - present	110	6.47×10^{-4}	6.6
Ruatoria Avalanche	0.17	0	0	0
Pre-Ruatoria unit	5 - 0.17	300	6.21×10^{-5}	5.2
Pelagic	120 - 5	605	5.26×10^{-6}	2.4
Total:	120	1015		14.3

Preferred sedimentation correction shows that the combined effects of the pelagic, pre-Ruatoria Avalanche unit, Ruatoria Avalanche, and post-Ruatoria Avalanche unit results in a sediment correction of 20.5 % being required. High sedimentation scenario reflects the likely upper bounds of sedimentation. The biggest difference relative to the preferred sedimentation correction is are a thicker Ruatoria Avalanche and overlying turbidite units. Low sedimentation correction scenario reflects the likely lower bounds of sedimentation. The biggest difference relative to the preferred sedimentation scenario is the absence of the Ruatoria Avalanche. These results indicate that the sedimentation correction is 20.5 % with conservative uncertainty of ± 7 %.

Table3. Material parameters of the 2-D finite element model used in this study.

Model unit	Thermal conductivity ($W\ m^{-1}\ K^{-1}$)	Volumetric heat capacity ($MJ\ K^{-1}\ m^{-3}$)	Heat generation ($\mu W\ m^{-3}$)
Sediment	1.5[a]	2.6[f]	0.69[h]
Accretionary prism	1.8[b]	2.6[f]	1.2[i]
Upper crust	2.1[c]	2.6[f]	1.8[j]
Lower crust	2.0[d]	2.6[f]	0.7[k]
Mantle wedge	3.1[e]	3.3[g]	0.006[l]
Lithosphere, oceanic crust, basement aquifer	3.1[e]	3.3[g]	0.006[l]

[a] Harmonic mean of 1200 m of sediment using porosity relation of Davis et al. 1999

[b] Mean of [a] and [c]

[c] Zoth and Hanel 1988, mean T = 200°C, acid rocks

[d] Zoth and Hanel 1988, mean T = 250 °C, acid rocks

[e] Stein and Stein 1992, Ellis et al. 2015, Harris et al. 2010, Currie et al. 2002, Hyndman and Wang 1993, Oleskevich et al. 1999

[f] He and Wang 2001

[g] Hyndman and Wang 1993, He and Wang 2001, Oleskevich et al., 1999

[h] ODP leg 181 site 1123 based on concentrations of K, U, and Th

[l] Fowler 2004, average between sediment and crust

[j] Fowler 2004, for average upper crust

[k] Fowler 2004, for average crust

[l] Fowler 2004, for peridotite

Table 4. Sensitivity of thermal regime to model parameters.

Parameter adjusted	Preferred value	Test	Movement from position at preferred value (km from deformation front)			Influence on heat flow
			100°C	150°C	350°C	(mW m^{-2})
Convergence velocity[a]	3.7 cm yr^{-1}	± 2.5%	± 0.2	± 0.3	± 0.5	< ± 0.2
Convergence velocity[b]	3.7 cm yr^{-1}	± 2.5%	± 0.5	± 0.5	--	< ± 0.2
Interface geometry[a]	0°	± 5°	± 0	± 1	+12, -25	< ± 3
Interface geometry[b]	0°	± 5°	± 0	+12, -6	--	< ± 3
Seaward geotherm[a]	120 Myr	+20%, -10%	± 0.4	± 0.5	± 0.4	< ± 0.3
Seaward geotherm[b]	120 Myr	+20%, -10%	± 0.4	< ± 0.75	--	< ± 0.5
Frictional shear velocity[a]	3.8 cm yr^{-1}	4.4 cm yr^{-1}	+2	+3	+5	< + 1
Frictional shear velocity[b]	3.8 cm yr^{-1}	4.4 cm yr^{-1}	+2	+2	+4	< + 1

[a] For $\mu' = 0.13$

[b] For $\mu' = 0.03$

2-D finite element subduction model parameters are adjusted during sensitivity tests. The preferred parameter values are shown, along with the range of variability tested, and respective resulting change in position of key isotherms along the subduction thrust fault.

12 Appendix

An array of bottom water temperature (BWT) instruments was deployed with absolute pressure gauges, ocean bottom seismometers, and as temperature moorings throughout the northern and southern Hikurangi Trough during cruise TAN 1405, onboard the R/V Tangaroa, 10 May 2014–20 May 2014. The temperature data shows strongly diminishing influence of bottom water temperature fluctuation, especially at depths greater than ~1000 m. Heat flow data strongly effected by bottom water temperature fluctuations is not presented not presented in this paper.

The heat flow probe used in this study measures temperature only at the time of penetration. The observed temperature gradient is a superposition of the background geothermal gradient and the temperature gradient due to the influence of BWT fluctuation at that time. BWT data can potentially be analyzed and used to correct the heat flow data under the condition that the temperature history recorded at the BWT site is representative of the temperature history at the heat flow measurement site.

The OBS sites were generally located on the order of 10's of kilometers away from heat flow measurement locations, bringing into question their ability to provide a suitable BWT gradient correction, as temperature history tends to deviate with distance. To evaluate if a regional model for the bottom water temperature can be developed and used to correct the observed temperature gradient, I analyzed the temperature data in several stages. A plot of standard deviations of temperature versus depth (Figure A1a) shows that standard deviation of the temperature fluctuations is inversely related to instrument depth, with standard deviations becoming very low (<0.07°C) at depths > 1500 m below sea level. Figure A1b shows the results of a cross correlation analysis on the time-series temperature data sets obtained at the BWT instrument locations. The horizontal axis in Figure A1b represents distance decomposed in the xy

directions, while colors represent distance decomposed in the z (depth) direction between BWT instrument pairs. In both cases, correlation decreases between BWT instruments as distance increases. A strong correlation exists only between temperature histories of several BWT instrument pairs that are similar in depth and proximal to one another, and these sites (correlation coefficient = 0.94) are much shallower and similar in depth (depth = 73–79.3 m) than heat flow measurements presented in this study. Generally, correlation reduces rapidly with increasing distance and depth difference. The lack of correlation between the bulk of the BWT instrument pairs precludes our ability to apply temperature histories from one site to other nearby sites. A regional bottom water temperature gradient model currently seems impossible to achieve.

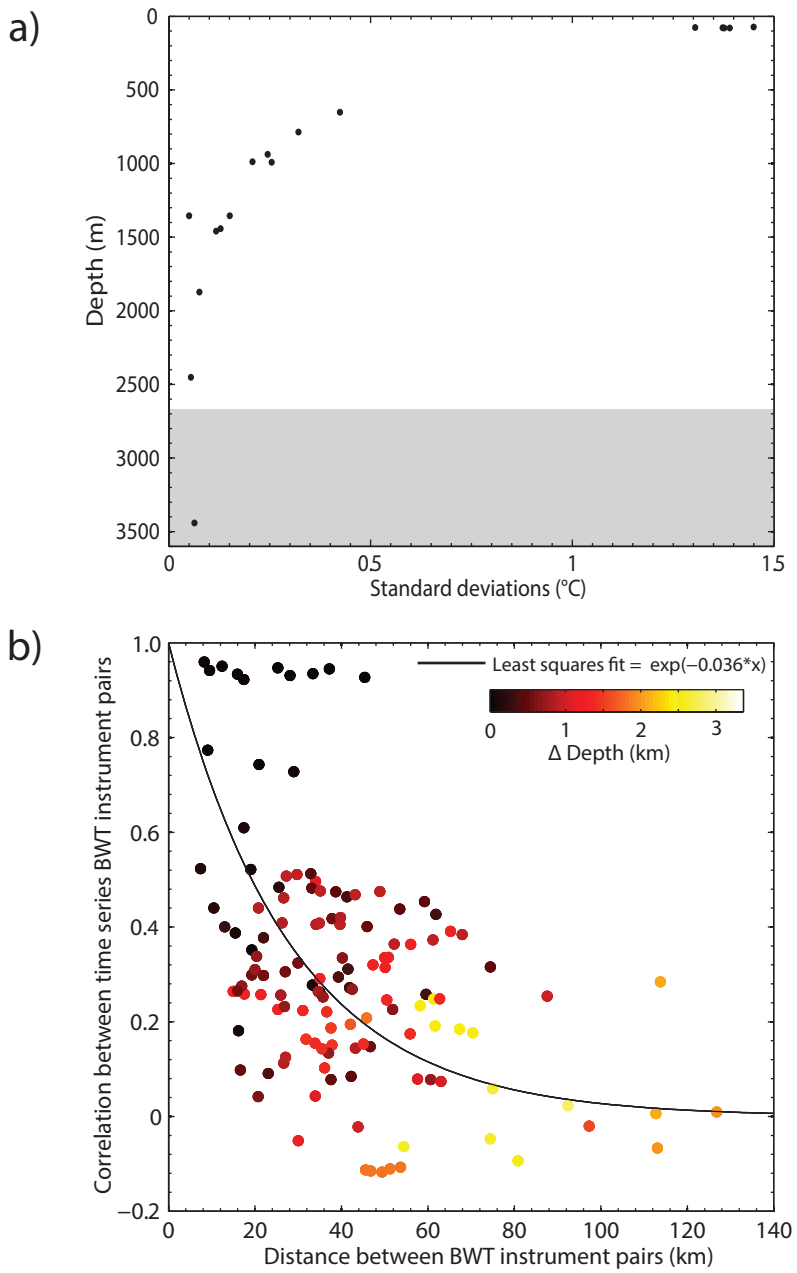

Figure 1. a) Standard deviation of 1-year of temperature-time series data from each of 19 bottom water temperature (BWT) instruments deployed in the Hikurangi Trough. An inverse correlation exists between instrument depth (vertical axis) and standard deviation (horizontal axis). Greyed zone represents depth range of heat flow measurements presented in this study. b) Cross correlations between 1-year temperature-time series data from pairs of BWT instruments in the Hikurangi Trough. The horizontal axis represents distance between BWT instrument pairs decomposed in the xy (map view) directions, while colors represent distance decomposed in the z (depth). An inverse relationship exists between cross correlation (vertical axis) and distance in the xy and z directions.